Geophysical Journal International

Geophys. J. Int. (2019) **216,** 1693–1710
Advance Access publication 2018 December 10
GJI Geodynamics and tectonics

doi: 10.1093/gji/ggy521

Lithospheric modification by extension and magmatism at the craton-orogenic boundary: North Tanzania Divergence, East Africa

C. Tiberi,[1] S. Gautier,[1] C. Ebinger,[2] S. Roecker,[3] M. Plasman,[1] J. Albaric,[4] J. Déverchère,[5] S. Peyrat,[1] J. Perrot,[5] R. Ferdinand Wambura,[6] M. Msabi,[7] A. Muzuka,[8] G. Mulibo[6] and G. Kianji[9]

[1] *Géosciences Montpellier, CNRS, Université de Montpellier, France. E-mail: Christel.Tiberi@umontpellier.fr*
[2] *Department of Earth and Environmental Sciences, Tulane University, New Orleans, LA 70118, USA*
[3] *Earth and Environmental Sciences, Rensselaer Polytechnic Institute, Troy, NY 12180, USA*
[4] *Laboratoire Chrono-environnement, Université de Franche-Comté, Besançon, France*
[5] *IUEM, Géosciences Océan, Plouzané, France*
[6] *Department of Geology, University of Dar es Salaam, Dar es Salaam, Tanzania*
[7] *College of Earth Siences, University of Dodoma, Dodoma, Tanzania*
[8] *WESE Department, Nelson Mandela African Institute of Science and Technology, Arusha, Tanzania*
[9] *Department of Earth Sciences, University of Uppsala, Uppsala, Sweden*

Accepted 2018 December 7. Received 2018 December 2; in original form 2018 April 27

SUMMARY

We present a joint analysis of newly acquired gravity and teleseismic data in the North Tanzanian Divergence, where the lithospheric break-up is at its earliest stage. The impact of a mantle upwelling in more mature branches of the East African Rift has been extensively studied at a lithospheric scale. However, few studies have been completed that relate the deep-seated mantle anomaly detected in broad regional seismic tomography with the surface deformation observed in the thick Archaean Pan-African suture zone located in North Tanzania. Our joint inversion closes the gap between local and regional geophysical studies, providing velocity and density structures from the surface down to *ca*. 250 km depth with new details. Our results support the idea of a broad mantle upwelling rising up to the lithosphere and creating a thermal modification along its path. However, our study clearly presents an increasing amplitude of the associated anomaly both in velocity and density above 200 km depth, which cannot be solely explained by a temperature rise. We infer from our images the combined impact of melt (2–3 per cent), composition and hydration that accompany the modification of a thick heterogenous cratonic lithosphere are a response to the hot mantle rising. The detailed images we obtained in density and velocity assert that Archaean and Proterozoic units interact with the mantle upwelling to restrict the lithosphere modifications within the Magadi–Natron–Manyara rift arm. The composition and hydration variations associated with those units equilibrate the thermal erosion of the craton root and allow for its stability between 100 and 200 km depth. Above 80 km depth, the crustal part is strongly affected by intruding bodies (melt and gas) which produces large negative anomalies in both velocity and density beneath the main magmatic centres. In addition to the global impact of a superplume, the velocity and density anomaly pattern suggests a 3-D distribution of the crust and mantle lithospheric stretching, which is likely to be controlled by inherited fabrics and enhanced by lateral compositional and hydration variations at the Tanzanian craton-orogenic belt boundary.

Key words: Gravity anomalies and Earth structure; Africa; Joint inversion; Seismic tomography; Intra-plate processes.

1 INTRODUCTION

Over its 3000 km of faulted, extended and intruded lithosphere, the East African Rift (EAR) alternates between mature and immature rifting zones, volcanic and non-volcanic areas (e.g. Pik *et al.* 2006; Fishwick & Bastow 2011). Geophysical data provides compelling evidence for a single thermal anomaly rising from the core–mantle boundary beneath southern Africa, but data gaps and variations

© The Author(s) 2018. Published by Oxford University Press on behalf of The Royal Astronomical Society.

Downloaded from https://academic.oup.com/gji/article-abstract/216/3/1693/5237708 by guest on 04 January 2019

in lithospheric structure complicate interpretations of the African Superplume through the transition zone (e.g. Hansen *et al.* 2012; Mulibo & Nyblade 2013; Thompson *et al.* 2015; Sun *et al.* 2017). The interaction between plume processes and the base of the heterogeneous continental lithosphere, and the importance of magma-enhanced rifting, therefore, remains debated. Magmatic modification of both crust and mantle lithosphere is well documented in the 15–20-Myr-old Main Ethiopian, Albertine and Kenya rift sectors (e.g. Bastow & Keir 2011; Lindenfeld & Rümpker 2011; Muirhead *et al.* 2015). Concerning the largely unstretched lithosphere at the edge of thick Archaean Tanzanian Craton, where extension started 7 Ma, the magma source zones and pathways to the crust was only weakly constrained by regional studies (e.g. Ritsema *et al.* 1998; Weeraratne *et al.* 2003).

The 2013-2015 CRAFTI and CoLiBrEA experiment (https://doi.org/10.7914/SN/XJ_2013) brings new insight to the questions of magmatic modification of the lithosphere during the initial stages of rifting, and the impact of lithospheric heterogeneities with detailed images of the North Tanzania Divergence (NTD). The NTD encompasses 0–6 Ma volcanoes, including the active carbonatitic Oldoinyo Lengai volcano, and many large offset border fault systems that formed in the past 3 Ma (e.g. Foster *et al.* 1997; Nonnotte *et al.* 2008; Mana *et al.* 2015). In this part of the rift, active faults and eruptive centres span the Archaean–Pan African suture and enable us to evaluate the role of pre-existing heterogeneities in mantle lithospheric thickness and composition based on Palaeozoic to present analyses of mantle xenoliths at the eruptive centres (e.g. Aulbach *et al.* 2008; Baptiste *et al.* 2015).

In this study, we combine gravity data measurements with teleseismic *P*-wave first arrival times in a joint inversion scheme to image the crustal and lithospheric structures in terms of coupled density and velocity structures. The combination of those two complementary data set will help to understand how inherited structures and Miocene–present magmatism interact in this complex active zone. Our results are interpreted in light of complementary crustal imaging studies of Roecker *et al.* (2017) and Plasman *et al.* (2017). Jointly inverting for density and seismic velocity brings new insights into rift evolution at the edge of a deeply rooted craton. We find evidence that the crust is extensively modified by magmatic intrusion in the northern part, while the southern part (Manyara) exhibits a contrasted high velocity but low density pattern which could act as a barrier for the rift propagation. Our results provide the appropriate scale to study how a deep seated mantle upwelling modifies a thick cratonic lithosphere, while bringing compelling evidence of lithospheric thinning, composition, hydration and temperature modification.

2 BACKGROUND

2.1 Tectonic and geodynamic

The NTD is part of the Eastern rift, one arm of the >3000-km-long East African rift system. Although no direct estimate of plate velocities is yet available, models of geodetic data indicate approximately E–W opening at rates less than 5 mm yr^{-1} (e.g. Saria *et al.* 2013; Stamps *et al.* 2018). Rifting initiated in Pan-African (late Proterozoic) and Archaean lithosphere, but the timing of the rift initiation varies significantly along the rift. In the northern part of the Eastern rift, magmatism and faulting initiated at ∼30 and ∼25 Ma, respectively, while magmatism in the NTD initiated at ∼6 Ma and faulting between ∼4 and 2 Ma (Le Gall *et al.* 2008; Mana *et al.* 2015; Baudouin *et al.* 2016).

The Eastern rift (or Kenya rift) is 50–80 km wide, but widens in northeastern Tanzania where faulting and magmatism occur across a 300-km-wide zone (fig. 1; Dawson 1992; Ebinger *et al.* 1997; Le Gall *et al.* 2008). Manyara–Natron–Magadi (MNM) rift zone lies between the Eyasi rift in Archaean craton to the west and the Pangani rift in Mozambique-belt lithosphere to the east (Fig. 1). The Masai block is a distinct crustal domain east of the Manyara rift, and its northern border roughly coincides with the sub-E–W Ngorongoro to Kilimanjaro volcanic chain. In this zone, volcanism started around 6 Ma (Dawson 1992; Mana *et al.* 2015), and shows a crude eastward younging pattern along the transverse volcanic belt between Ngorongoro and Kilimanjaro (Mana *et al.* 2015), which also includes Monduli, Meru volcanoes and the still active Oldoynio Lengai (Fig. 1). Basin subsidence and rift flank uplift had initiated by 3 Ma in the Natron–Magadi area, but much of the present basin structure was formed over the past 1 Ma (Foster *et al.* 1997; Le Gall *et al.* 2008; McHenry *et al.* 2011). Two isolated edifices (Kwahara and Hanang) can be found further south and southwest of Lake Manyara, near the craton suture (Fig. 1).

Crust and mantle xenolith data indicate that Archaean mantle lithosphere underlies thin-skinned thrusts of the Pan-African orogen and that much of the Natron–Manyara rift zone formed above Archaean mantle lithosphere (Vauchez *et al.* 2005; Aulbach *et al.* 2008; Baptiste *et al.* 2015). Active deformation and volcanic eruptions in 2007–2008 provide compelling evidence for the participation of magma intrusion in strain accommodation, in addition to slip on large offset faults in the early stage of rifting (Baer *et al.* 2008; Calais *et al.* 2008; Biggs *et al.* 2009; Albaric *et al.* 2010). The Manyara rift segment, which lacks Holocene eruptive centres in its central part, is the location of deep (>20 km) and persistent seismicity (Nyblade *et al.* 1996; Albaric *et al.* 2010; Yang & Chen 2010). Deep seismicity also occurs in the central Natron and Magadi basin segments, which are the sites of ongoing magmatic underplating and intrusion as indicated by crustal imaging and active CO_2 degassing along major faults (Seht *et al.* 2001; Lee *et al.* 2016; Plasman *et al.* 2017; Roecker *et al.* 2017; Weinstein *et al.* 2017).

2.2 Previous geophysical work

Previous geophysical studies in Kenya and Tanzania have demonstrated the presence of a low seismic velocity upper mantle beneath the eastern branch extending to depths of at least 400–500 km (Ritsema *et al.* 1998; Mulibo & Nyblade 2013). This low velocity pattern is consistent with a *ca*. 300 K thermal or composition perturbation and is often associated with the African superplume influence. The broad uplift and corresponding negative free air gravity anomaly, and the deep low-velocity zone are attributed to a deeply sourced mantle plume (e.g. Ebinger & Sleep 1998; Huerta *et al.* 2009; Adams *et al.* 2012; Mulibo & Nyblade 2013). Large scale gravity and seismic studies indicate that the cratonic lithosphere is much stronger and thicker than the Pan-African lithosphere (e.g. Petit & Ebinger 2000; Pérez-Gussinyé *et al.* 2009), and that the entire region is underlain by a low velocity, low density mantle (e.g. Weeraratne *et al.* 2003; Fishwick & Bastow 2011; O'Donnell *et al.* 2013). The coarse scale of those regional studies prevents the determination of the shape of the craton/hot mantle boundary, even if mantle tomographic images show a generally west dipping low velocity body under the Tanzanian Craton (Ritsema *et al.* 1998;

Downloaded from https://academic.oup.com/gji/article-abstract/216/3/1693/5237708 by guest on 04 January 2019

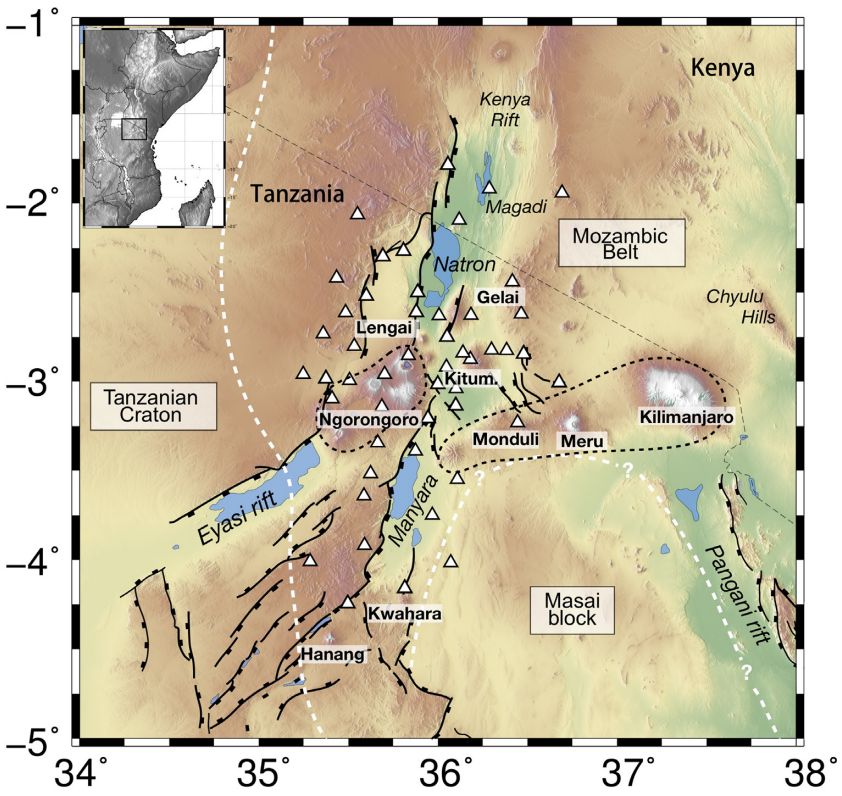


Figure 1. Location of the seismic network (2013–2015, white triangles) on the topographic (SRTM3) map of the study area. Main geological and volcanic features are indicated and taken from Albaric *et al.* (2014). Presumed Tanzanian Craton and Masai block limits are outlined by dashed white line. Volcanic edifices names are noted in bold, and main volcanic axes are surrounded by black dashed lines. Ticked black lines indicate major faults.

Achauer & Masson 2002). The contrast between cratonic and mobile belt lithosphere is also imaged in magnetotellutic studies, where the electrical conductivity is used as a proxy for hydrogen content (Selway *et al.* 2014; Selway 2015). From xenolith analyses, the Tanzanian Craton is one of the driest craton (Hui *et al.* 2015) but seems to be H-richer (hence more resistive) compared to the mobile belt at 100–160 km depth.

The resistive structure of the Kenya Rift appears to be highly heterogeneous with a strong 3-D pattern linked to the interaction between pre-existing lithospheric thickness and rheology variations between the Archaean craton and thinner Mozambiquan orogenic belt (Simpson 2000). Low resistant zones has been pointed out beneath the Chyulu Hills in the upper (<8 km) and middle (8–18 km) crust (fig. 1, Sakkas *et al.* 2002). They have been interpreted as melt pockets derived from the main Kenya Rift valley, and promote potential lateral extension of a broader mantle upwelling. Passive and active crustal imaging of the Natron–Manyara region indicates a heterogeneous crust, with highly variable lower crustal velocity and *Vp*/*Vs* ratio (Birt *et al.* 1997; Albaric *et al.* 2014; Roecker *et al.* 2017). The Moho depth variation ranges from 27 to 40 km, and lower crust and upper mantle low velocity interfaces are interpreted to be the focus of either melt or localized deformation zones (Birt *et al.* 1997; Plasman *et al.* 2017). Heat flow is high but spatially variable within the Magadi Basin, suggesting advective transfer by magmatism and hydrothermal fluids (Nyblade *et al.* 1990; Wheildon *et al.* 1994). Active volatile degassing along border faults which lower crustal projections are associated with deep earthquakes are consistent with active magma intrusion into the lower crust (Lee *et al.* 2016; Weinstein *et al.* 2017).

Investigating the intermediate scale between local and regional previous analyses in this magmatic segment of the EAR is a unique opportunity to shade light on the processes involved into the deformation in the early stage of continental rifting, and to explore the link between mantle and crustal interactions.

3 DATA AND METHODS

3.1 Gravity and seismic data sets

We gather gravity data from the Bureau Gravimetrique International (BGI) and 178 new data collected between 2013 and 2015 in Natron–Manyara region in the framework of the CoLiBrEA project (Fig. 2). The global data set, inverted for gravimetry, is composed of 14 745 points of Bouguer anomaly, calculated relative to the International Association of Geodesy 1967 formula. The average density of 2.67 g cm^{-3} is used to correct for topography. The complete Bouguer correction was performed by applying a ground correction derived from a 90 m resolution digital elevation model (SRTM90). We apply a 5 km upward continuation to filter out the shortest wavelengths related to crustal smallest anomalies. This increases the coherency between gravity and seismic data sets (Fig. 2b). The distribution of gravity data in the study area is strongly irregular due to the lack of passable roads. The large width of uncovered zones does not allow us to grid the Bouguer anomaly without including artificial signal. We then invert the data at their real location to preserve spatial information and data coverage.

For seismic data, we use traveltimes from teleseismic events recorded by 45 temporary broad-band stations of CRAFTI-CoLiBrEA networks deployed between January 2013 and May 2015

Downloaded from https://academic.oup.com/gji/article-abstract/216/3/1693/5237708 by guest on 04 January 2019

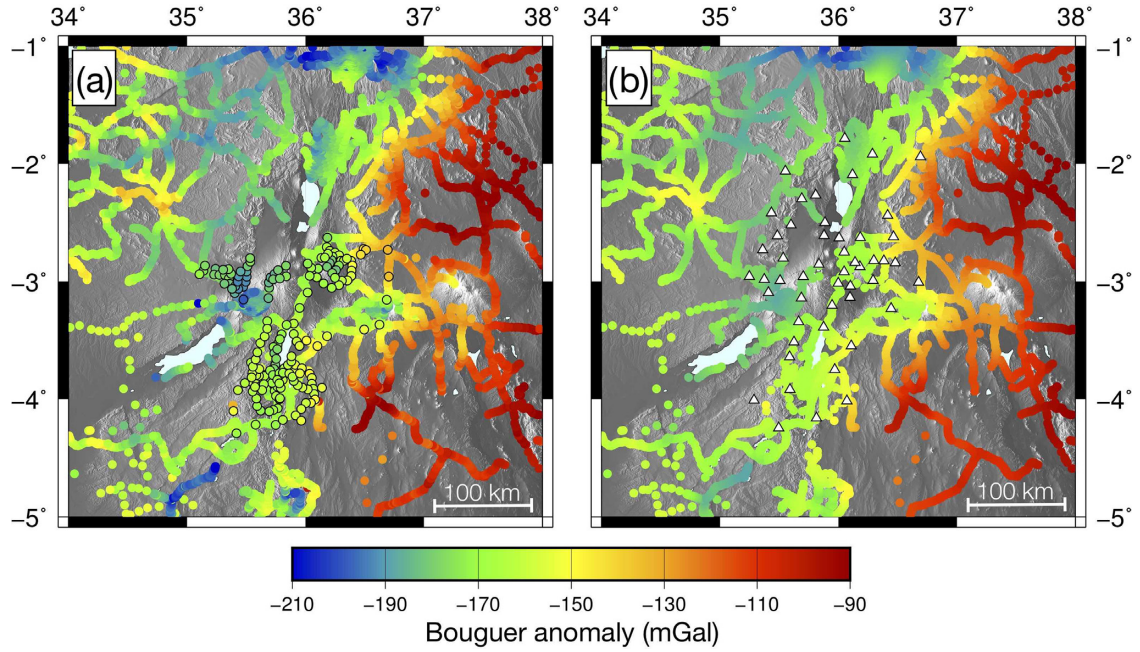


Figure 2. (a) Complete measured Bouguer anomaly in the study area from BGI and from this study (black circled points). (b) Upward continuation of (a) by 5 km in order to reduce the shortest wavelengths in the signal. The seismic stations are indicated by white triangles.

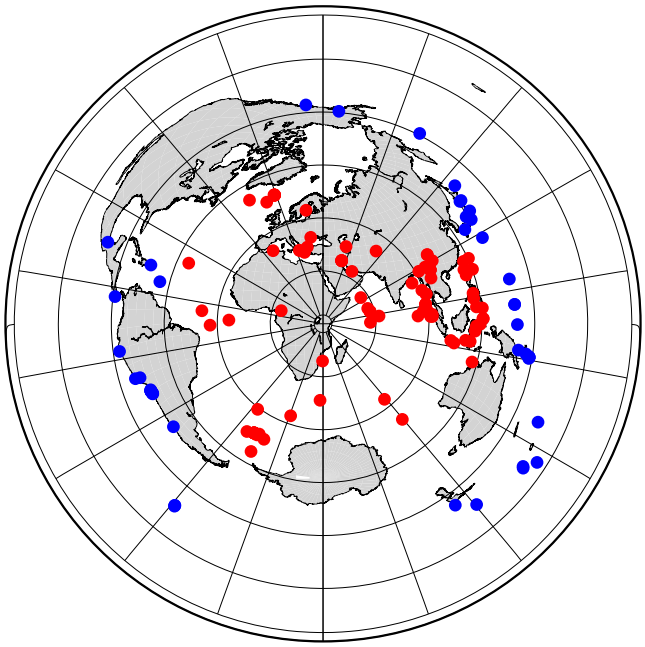


Figure 3. Azimuthal distribution of the 160 events used for the travel time inversion. The red circles are epicentres for first *P*-wave arrival events and the blue ones refer to the PP first arrival events. The projection is centred on the network.

in the Magadi, Natron and Manyara rift segments (Figs 1 and 3). The network was composed of Reftek recorders coupled with STS2, CMG40 or Trillium sensors (Roecker *et al.* 2017). The ten stations in the central and southern Manyara basin, which recorded for only 9 months, were composed of Osiris datalogger connected to short period Neomax sensors. All stations were powered by batteries charged with solar panels and the time was provided by GPS. We selected 160 earthquakes of $M_b > 6.0$ with epicentral distances ranging [25–90°] for *P* waves and [90–180°] for *PP* waves (Fig. 3) for the period 2014–2015. Events from 2013 were not used because of nearly network-wide GPS clock failures between January and December, 2013, and the complexity of timing corrections (Roecker *et al.* 2017). We filtered waveforms with a two-pass Butterworth filter with corner frequencies of 0.08 and 0.8 Hz and picked the *P* waves on the vertical component seismograms. We used a cross-correlation technique based on VanDecar & Crosson (1990) to compute the traveltime residuals relative to IASP91 reference arrival time (Kennett & Engdahl 1991; Tiberi *et al.* 2000). This semi-automatic method estimates the picking uncertainty from the standard deviation of the cross-correlation function, which in our case ranges between *ca.* 0.02 and 0.17 s. In total we input 4047 residual times in our joint inversion with a reasonably homogeneous azimuthal distribution. Due to the natural distribution of seismicity, most of the events are coming from the northeast quadrant (Fig. 3). However, PP events complete the western part and improve the distribution. The mean relative residuals range from –1.6 to 1.1 s, and underlie a very heterogeneous lithosphere with strong velocity contrasts (e.g. Evans & Achauer 1993; Bastow *et al.* 2008; Mulibo & Nyblade 2013).

3.2 Joint inversion and parametrization

The method we used is based on the joint inversion scheme of Zeyen & Achauer (1997) modified by Tiberi *et al.* (2001). This Bayesian approach fully combines the two data sets and includes *a priori* information by the way of initial input models of gravity and seismic velocity, smoothing constraints, *a priori* model and data standard errors. The inversion proceeds iteratively until the sum of the difference between observed and calculated data reaches a given threshold (set to 0.3) or when the maximum number of iterations is reached (set here to 5). After testing different geometries, we set the seismic and density models to be composed of seven common layers (0–40–80–135–185–235–270 km depth), which optimize together the ray coverage, the gravity frequency content and the resolution with depth (e.g. Zeyen & Achauer 1997). Seismic velocities are

Downloaded from https://academic.oup.com/gji/article-abstract/216/3/1693/5237708 by guest on 04 January 2019

assigned to nodes. Each layer contains 21x25 nodes in the EW and NS directions, respectively. The velocity nodes spacing was chosen to correspond to the average seismic station spacing, that is 25 km. The a priori velocity model is based on typical values in a homogeneous lithosphere, which is derived from IASP91 model (Kennett & Engdahl 1991). The gravity model is made of 23x25 rectangular blocks in each layer, in EW and NS direction, respectively. A density contrast is assigned to each block, and the starting model is based on typical homogeneous density values (Dziewonski & Anderson 1981). To ensure the coherency between the two models, each velocity node corresponds to a density block. Wider density blocks are added in the EW and NS directions to absorb the boundary effects. We link seismic velocity with density using Birch's law (Birch 1961):

$$\Delta V_p = B.\Delta\rho.$$

Even if it has been empirically determined, it is widely accepted as a good approximation of a power law derived from lattice dynamics over the density range [2500–4000 kg m^{-3}] within which our model rocks vary (Chung 1972). In this approach B, is a parameter which can be inverted (Tiberi *et al.* 2001). However, this consideration makes the inversion non-linear and unstable. To reduce this, we restrict the possible value for B into a reasonable range (Birch 1961; Christensen & Mooney 1995) and use a small *a priori* standard deviation for it (0.1 km s^{-1} g^{-1} cm^3).

We obtained the most suitable parametrization for our region after testing various combinations for the inversion process factors (smoothing, size of the grids, initial model standard deviation, number of iterations, data covariance) Theoretically, our inverse problem contains 8547 parameters to estimate. However, because we will only consider velocity nodes with three rays in their vicinity to be inverted, this number is reduced to 5759. We estimate the success of the inversion through the rms decrease between observed and calculated data, and the final standard deviation of the parameters and the calculated data. Results harmonizing significant RMS decrease with realistic calculated data and parameter standard deviations are obtained for a smoothness constraint of 0.8 and 0.1 for density and velocity, respectively. In the final stage, we proceeded to 5 iterations, after which we obtained a RMS decrease of 96.8 per cent for the gravity data (37.98–1.21 mGal) and 41.2 per cent for the delaytimes data (0.28–0.16 s, Fig. 4). The standard deviations of calculated data are 37.95 mGal and 0.23 s for gravity and delaytimes, respectively. Those values are highly comparable to the observed one and reflect an overall similar distribution (37.98 mGal and 0.28 s). The rms decrease is smaller in seismic than in gravity, as usually observed in those joint inversions (e.g. O'Donnell *et al.* 2013). First, gravity inversion is more linear than the seismic process, and thus converges more efficiently to a stable solution. Second, our obtained seismic rms decrease is very similar to the ones retrieved in other seismic or joint inversions and seems to be in a typical range of values (e.g. Gautier *et al.* 2006; Roecker *et al.* 2017). The gravity data are retrieved within 1 or 2 mGals except for a few local values (Fig. 4a).

4 RESULTS

Before presenting our results, we estimate the capability of our inversion to correctly restore the lithospheric velocity and density distribution. We first use the azimuthal distribution of the seismic events as a proxy for the resolving power of the inversion, because it controls the ray coverage within the velocity model. The resolution of our velocity model is better in the northeast compared to the southwest, because a majority of arrivals are from the northeast direction causing an uneven distribution of seismic events (Fig. 3). When studying the piercing points distribution through the specific layers of our model, this azimuthal bias expands as we go deeper, inducing a decreased resolution beneath the central part of our network below 200 km depth (Fig. 5). We thus expect to underestimate velocity contrasts for the central part of the model from this depth and below. The addition of gravity data in the inversion scheme counteracts the lack of seismic rays in some regions. Particularly in the southernmost part of the model, where the amount of seismic data has been reduced due to the shortened recording period, the gravity data coverage enhances the resolution power at lithospheric depth. Lastly, the diagonal terms of the resolution matrix shows reasonable values until 235 km (layer 6), with maximum terms shifted to the NE as we go deeper (Fig. 5). It simply reflects the uneven ray distribution.

4.1 Resolution tests

We test the resolution our models can achieve through different synthetic tests.

A well-known artefact in the teleseismic inversion is the smearing of the information along the quasi-vertical rays. The velocity anomalies are spread over the layers and the amplitude can be significantly decreased within each of them (e.g. Bastow *et al.* 2008). As a standard estimate for this effect, we first perform checkerboard tests in different layers. The input anomalies are ±5 per cent in velocity and density compared to the background values. They are 2x2 nodes or blocks, that is 50 km by 50 km wide. The output models clearly show that the checker pattern, is retrieved both in amplitude and place for density and velocity, while the smearing effect is the largest in the layers above and below the input anomaly depth (Figs 6 and 7). Those tests further illustrate the interplay between velocity and density inversions. While the density resolution is not restricted to the central part of the network as the data coverage is wider, the velocity reconstruction greatly helps to localize the density anomalies at the correct depth (Fig. 8). Note that the lateral smearing effect coming from the seismic ray path distribution propagates within the density model, where we expect a better lateral resolution (Fig. 9). Conversely, the depth smearing is considerably reduced for the density model in the first layer compared to the velocity (Figs 8 and 9).

Checkerboard tests are not representative of real structures in the lithosphere, and to this point may not completely reflect the resolving power of our inversion for real anomalies. We conducted spike tests with two separate but close anomalies for layers 2 and 5 (40 and 185 km depth). They are 5 per cent slower and less dense than the surrounding velocity and density, respectively. They are 50 km wide and separated by only one node/block (i.e. 25 km), the smallest distance we can model. Similarly to the checkerboard, the outputs evidence blurring velocity and density variations within the adjacent layers, with a smaller amplitude in density for the first layer and a widening effect with depth (Figs S1 and S2). However, the maximum amplitude is located at the correct depth, and the separation between the two bodies is also accurately recovered. The shape of the two adjacent anomalies is remarkably restored, which is usually problematic for negative anomalies (Steck & Prothero 1991). The results of those tests demonstrate that if negative anomalies are present, even in the deepest part of our model, they could be

Downloaded from https://academic.oup.com/gji/article-abstract/216/3/1693/5237708 by guest on 04 January 2019

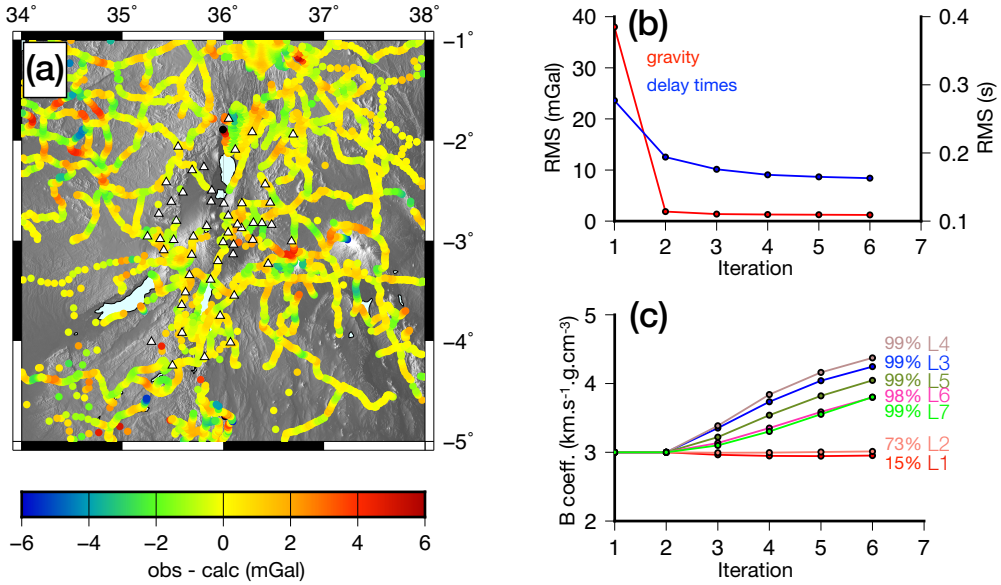


Figure 4. (a) Difference between gravity data and the recovered ones from the inversion (Observed - calculated) (b) rms decrease for gravity (red) and delaytimes data (blue). (c) B-coefficient evolution through the inversion iterations. The final correlation coefficient is indicated with the colour corresponding to the layer at the end of the curves. L*n* indicates the layer number.

efficiently resolved in shape and amplitude by the joint inversion. Vertical blurring effects are present but seems to be limited in the contiguous layers. Thus, we are confident that any structure larger than 50 km can be resolved independently from adjacent structures.

4.2 Velocity–density relationship

The obtained density and velocity values from our joint inversion range between reasonable values for such geodynamic region ($\pm$0.6 g cm^3 for density and $\pm$5 per cent for velocity, Figs 10 and 11).

The *B* values we obtained for layers at 0 and 40 km depth (2.9 and 3.0 m s^{-1} g^{-1} cm^3, respectively) are similar to agreed estimates in the crust and uppermost mantle (e.g. Birch 1961; Christensen & Mooney 1995). For depths greater than 80 km, *B* exceeds 4 m s^{-1} g^{-1} cm^3, a critical value for which the linear approximation made in Birch's law may not be valid (Chung 1972).

The correlation between velocity and density through each layer can be checked (Fig. 4c). The correlation is poor for the shallowest layers (<50 km) and reaches 75 per cent at 30 km depth. This reflects a strong disparity between velocity and density in the crustal part of the models (Figs 12 and 13). This is not surprising given that the strongest compositional variations are largely restricted to the crust, inducing strong deviations in the velocity–density relationship (Chung 1972). For a crustal image of density and velocity variations, one can refer to Roecker *et al.* (2017). They coupled the gravity and arrival time inversions using two general and crustal rocks derived relationships for the whole model down to 40 km (Roecker *et al.* 2004). Their study serves as a calibration with our results, which have marginal resolution in the upper 40 km. For the deepest layers (from 30 to 300 km), the correlation increases rapidly to reach more than 95 per cent (Fig. 4) and is transcribed by a more coherent and long wavelength feature in the two models (Figs 10 and 11). This strong coherency *a posteriori* legitimises the use of a single simple Birch's law over the lithosphere–asthenosphere density range [2.5–4.0 g.cm^{-3}]. It consolidates the idea that even if the physics behind it is not yet understood, this linear relationship between density and velocity approximates power law resulting from lattice dynamics over a given density range (Chung 1972).

4.3 Velocity and density structure

From a crustal point of view ($\leq$40 km), our resulting anomalies display smaller amplitudes than the recent local crustal tomography studies (Albaric *et al.* 2014; Roecker *et al.* 2017). We relate this observation first to the smearing effect, which is responsible for a decay of values the deeper we image. Second, we regularize the inversion with a damping factor, which counteracts the strongest anomalies occurring within the crust. For depth less than 30 km, where strong lateral anomalies are imaged (Roecker *et al.* 2017), the use of a damping factor helps us avoid mapping those heterogeneities to deeper layers. Within the crust, low velocity and density zones dominate the centre part of the models with a strong 3-D distribution (Figs 10 and 11), similar to recent local tomography (Roecker *et al.* 2017). Those negative anomalies align with the location of volcanic edifices, such as Ngorongoro Crater Highlands, Lengai and Meru (Fig. 1). These low density and velocity areas broaden northward, whereas they are bounded south, east and west by strong positive bodies at 40 and 80 km depth.

Below 80 km depth, those negative areas merge to form a large and unique low velocity and density zone. Its maximum amplitude is located at *ca.* 100–200 km depth and reaches –5 per cent in velocity and –0.06 g cm^{-3} in density (Figs 10 and 11). Down to 150 km, this anomaly is very narrow in the EW direction (*ca.* 100 km), and steep-sided by two denser (+0.06 g cm^{-3}) and faster (+4–5 per cent) bodies located beneath the Tanzanian Craton and the Mobile Belt (Fig. 12). Below 200 km depth, the Pangani region is associated with an eastward continuation of this low velocity and density body (–3 per cent in velocity and –0.04 g cm^{-3} for density, Figs 10 and 11). This is consistent with a local low velocity zone detected beneath station KOMO (Julià *et al.* 2005). Our results demonstrate a broadening of this anomaly. The Pangani Branch, of

Downloaded from https://academic.oup.com/gji/article-abstract/216/3/1693/5237708 by guest on 04 January 2019

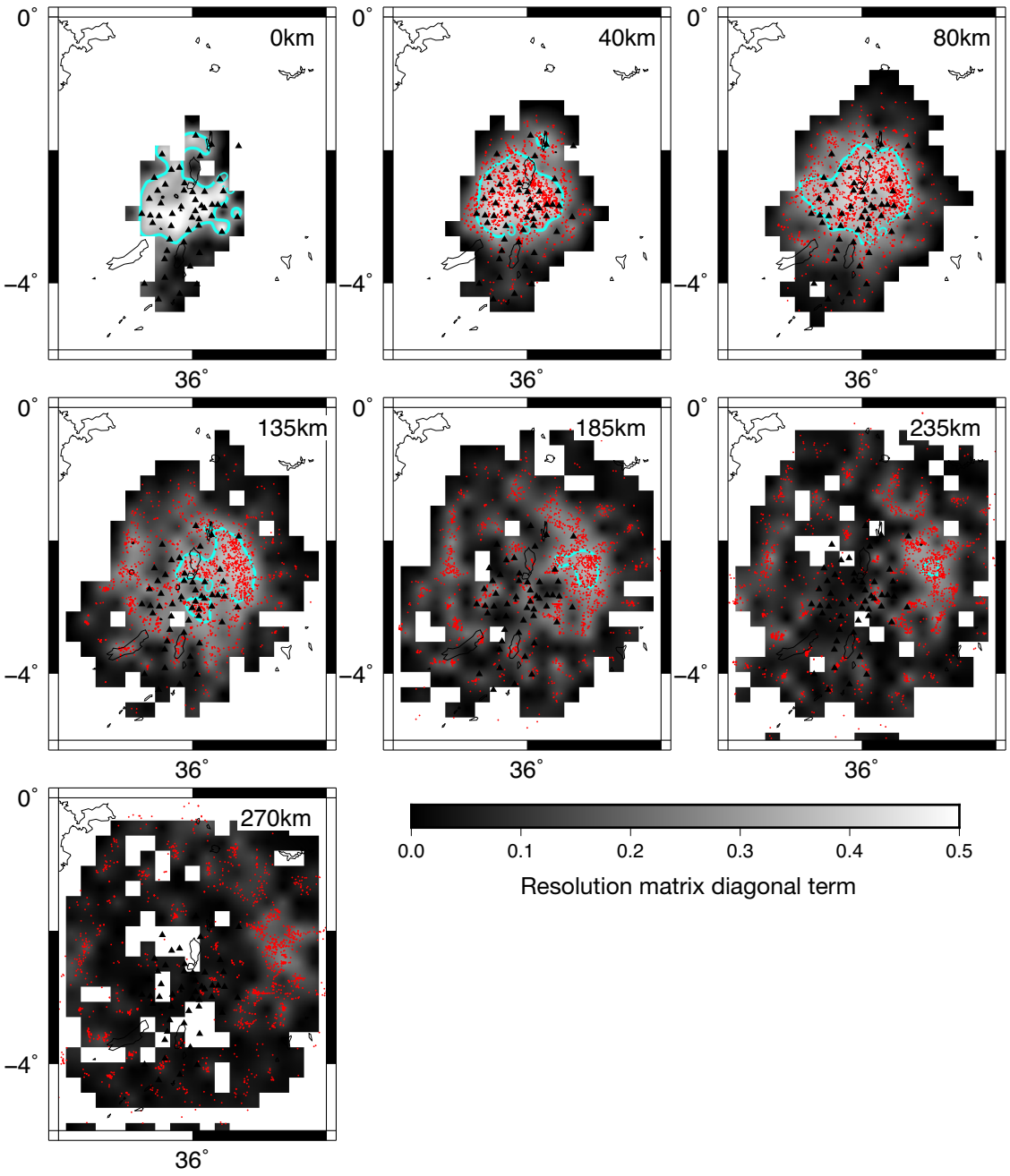


Figure 5. Resolution map for the velocity model. The gray scale represent the diagonal term of the resolution matrix (max=1), and the red points display the piercing points of the teleseismic rays at the associated layer depth. The thick blue line represents 0.5 value contour in resolution matrix diagonal terms. White areas are zones where nodes are not inverted due to a lack of ray crossing.

the NTD, is associated to an asthenospheric anomaly of small extent, which can explain the limited amount of magmatism and faulting in this zone (Mulibo & Nyblade 2016; Weinstein *et al.* 2017).

Synthetic tests indicate that the best lateral resolution of our models is between 50 and 200 km, including negative bodies (Figs S1 and S2). We are confident that both amplitude and lateral location of these anomalous bodies are correctly reproduced within those depths. We also estimated the effect of a negative anomaly located outside our model depth limit. The supporting information, Fig. S3, shows that such a body will only partially spread upward (max. –2 per cent retrieved at 185 km for an initial –5 per cent velocity anomaly at 300 km). Its effect is thus added to the already existing anomalies, while the amplitude at 270 km is underestimated by a factor of 2 or 3 (Fig. S3). Therefore, we cannot assess the continuity at depth for the negative central anomaly modelled. The signal imaged at 270 km is either the artificial downward propagation of a low density and velocity body stopping at 250 km (vertical smearing), or the partial image of a continuous anomaly from the lithosphere down to the transition zone.

Our models clearly associate the Tanzanian Craton and Mobile Belt major units with strong positive density (up to +0.06 g cm^{-3}) and velocity anomalies (+4–5 per cent) from 40 km down to *ca.* 200 km depth (Fig. 12). A similar positive anomaly, though less intense (+2 per cent in velocity and +0.03 g cm^{-3}), is observed

Downloaded from https://academic.oup.com/gji/article-abstract/216/3/1693/5237708 by guest on 04 January 2019

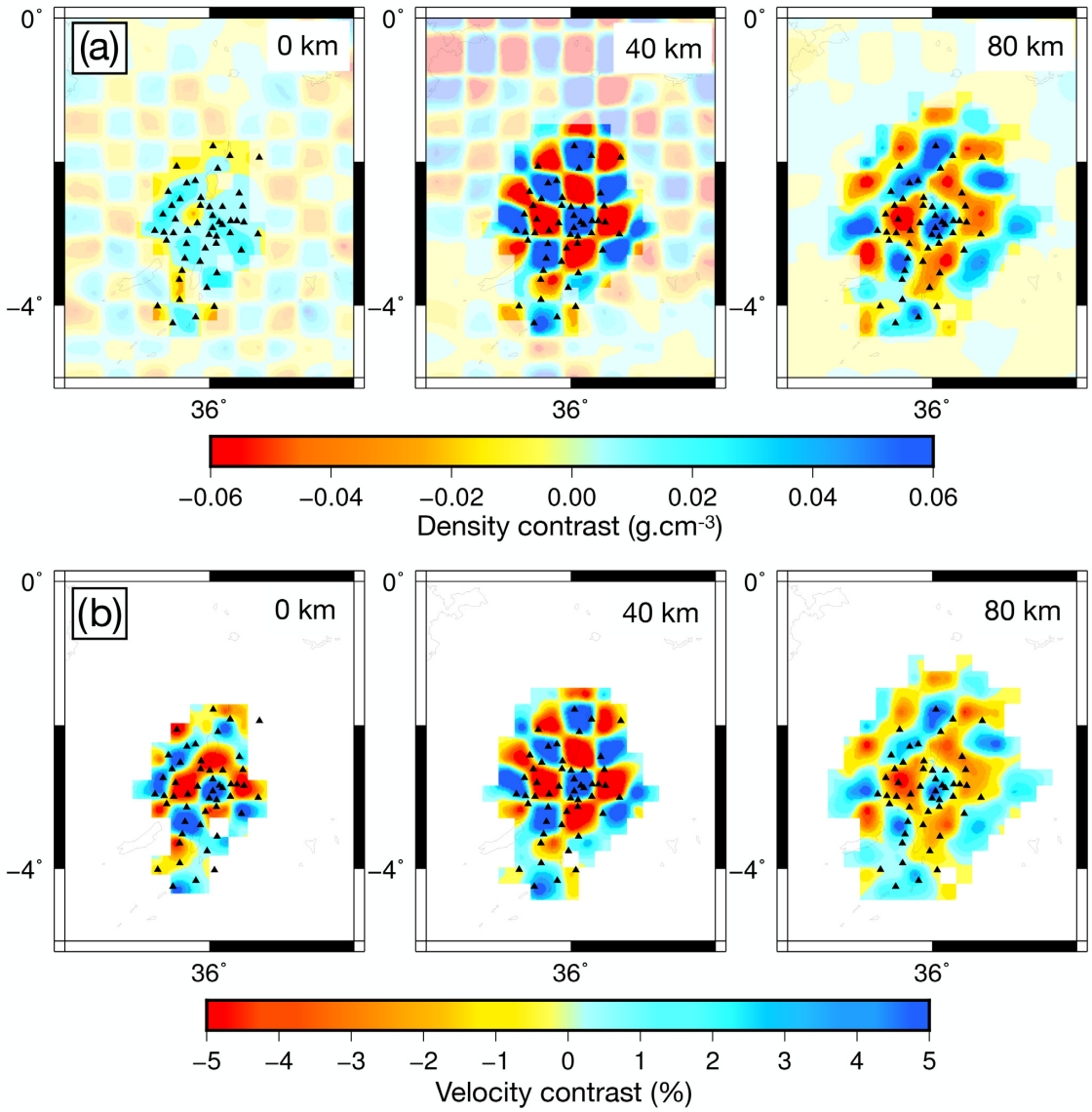


Figure 6. Result from checkerboard test with ±5 per cent anomalies in layer 2 (40 km depth), for (a) the density contrast and (b) the velocity anomaly. The transparency mask in (a) indicates zones not constrained by seismic rays.

southeast of the network, beneath the Masai block from *ca*. 80 down to 185 km (Figs 10 and 11). The crust beneath the Manyara rift exhibits a clear and well resolved negative density but positive velocity anomaly (Fig. 13), while previous magnetotelluric studies evidence a slightly more conductive pattern (Selway 2015). This contrasted geophysical signature enlightens the existence of a distinct unit separating the Tanzanian Craton and the Masai block. This particular domain is referred to as the Mbulu domain in Albaric *et al.* (2014) and corresponds to highly deformed Proterozoic structures (Le Gall *et al.* 2008). Its heterogeneous structure may have favoured the location of surface deformation and participate to the location and propagation of the Manyara rift Branch in the MNM area (Ebinger *et al.* 1997; Le Gall *et al.* 2008).

5 DISCUSSION

Large scale tomographic studies enable us to draw a mantle scenario and propose a mantle plume impingement to explain the observations in the Eastern Branch of East African Rift (e.g. Ritsema *et al.* 1999; Huerta *et al.* 2009). However, the thermal and compositional variations in lithospheric structure related to this mantle upwelling, the thermal state and the composition modification of the first 100s of km are still largely speculative, considering the sparse data coverage. By imaging the lithosphere and asthenosphere structures down to 300 km, our combined density and velocity models close the gap between local crustal and regional mantle studies. Our study allows us to identify the combination of factors, primarily temperature, hydration and composition, that control the deformation of this stretched and thick cratonic lithosphere.

Downloaded from https://academic.oup.com/gji/article-abstract/216/3/1693/5237708 by guest on 04 January 2019

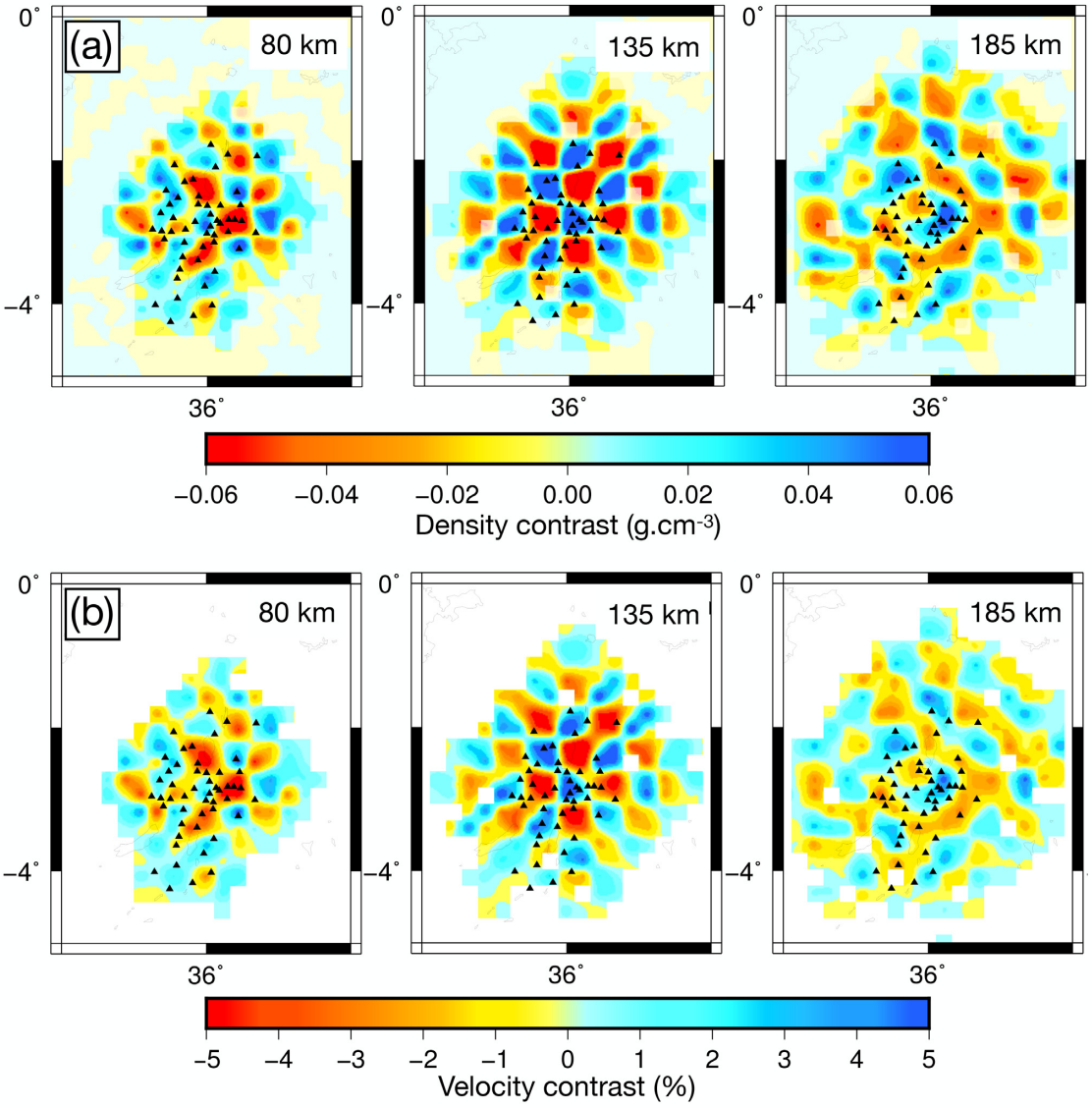


Figure 7. Result from checkerboard test with ±5 per cent anomalies in layer 4 (135 km depth), for (a) the density contrast and (b) the velocity anomaly. The transparency mask in (a) indicates zones not constrained by seismic rays.

5.1 Connection with a broad mantle upwelling

Larger tomographic studies in the Eastern Branch suggest a broad low velocity zone rising from the core mantle boundary (Ritsema *et al.* 1998; Huerta *et al.* 2009; Mulibo & Nyblade 2013b; French & Romanowicz 2015; Garnero *et al.* 2016), and most interpretations relate the uplift and deformation observed at the surface to the impingement of a mantle upwelling, like other regions of the East African Rift (Benoit *et al.* 2006; Fishwick 2010). We image a similar low velocity and density region just below the MNM rift zone, but with a higher amplitude than those obtained for more regional models (Ritsema *et al.* 1998; Mulibo & Nyblade 2013). Its strong amplitude (-5 per cent and -0.06 g.cm^{-1}) and narrow geometry are clear from 40 km down to 180 km, where the resolving power of our inversion is the best. However, below 200 km, the amplitudes of density and velocity anomalies decrease while the ray coverage scatters (Figs 10 and 11). This pattern can be produced by a downward smearing from a body limited to the first 180 km, as shown in our synthetic test (Fig. S2). We can then question the continuity of this body deeper in the mantle, and its connection with a regional mantle upwelling. We could consider that the central low velocity and density anomaly we image in our models extends deeper, but is not correctly recovered by our inversion between 180 and 270 km due to the decreased resolving power with depth. However, synthetic tests displayed in supplementary materials (Figs S4 and S5) shows that a -5 per cent anomalous and continuous body from a depth of 80 km down to 300 km creates even more scattered ray distribution, together with a higher amplitude recovery, contradictory to what we actually observed. The modelling results indicate that the continuation of this central anomaly below 200 km is subject to a reduction in amplitude, which agrees with mantle velocity values of other mantle tomography studies for depth greater than 100 km (max ±1.5 per cent, Mulibo & Nyblade (2013)). It also implies that multiple factors are then responsible for the increase of amplitude in ours models above 200 km.

Downloaded from https://academic.oup.com/gji/article-abstract/216/3/1693/5237708 by guest on 04 January 2019

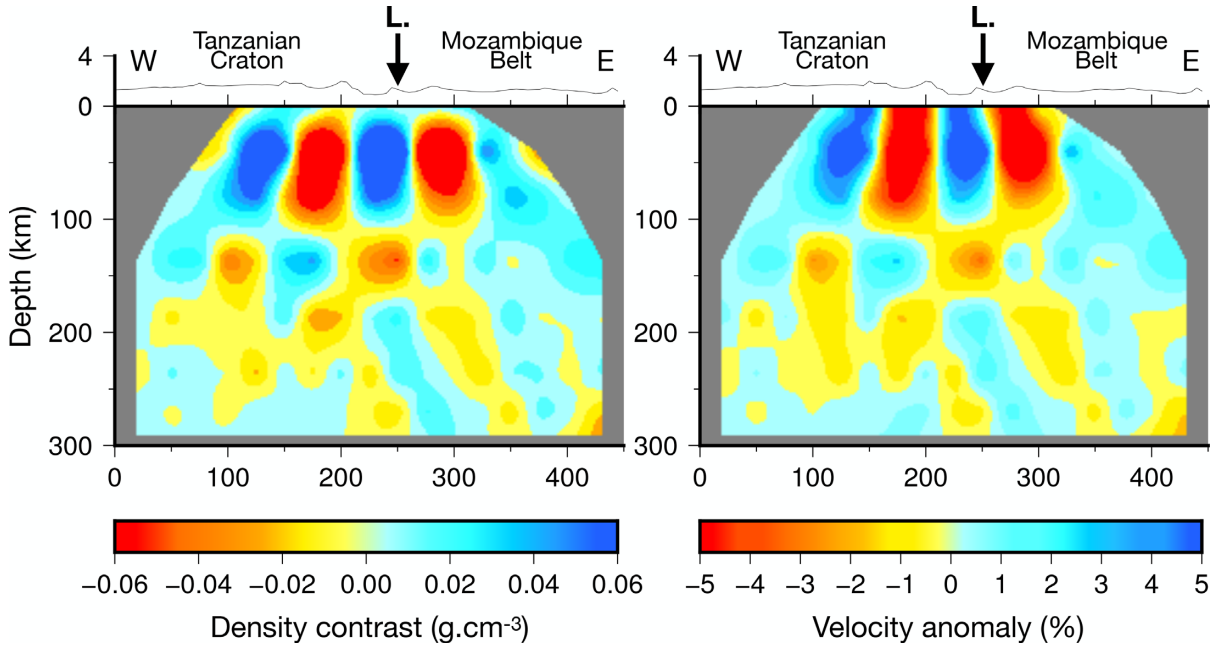


Figure 8. Density and velocity cross-sections for the checkerboard test with ±5 per cent anomalies in layer 2 (40 km depth). The profile is EW oriented at –2.8 latitude.

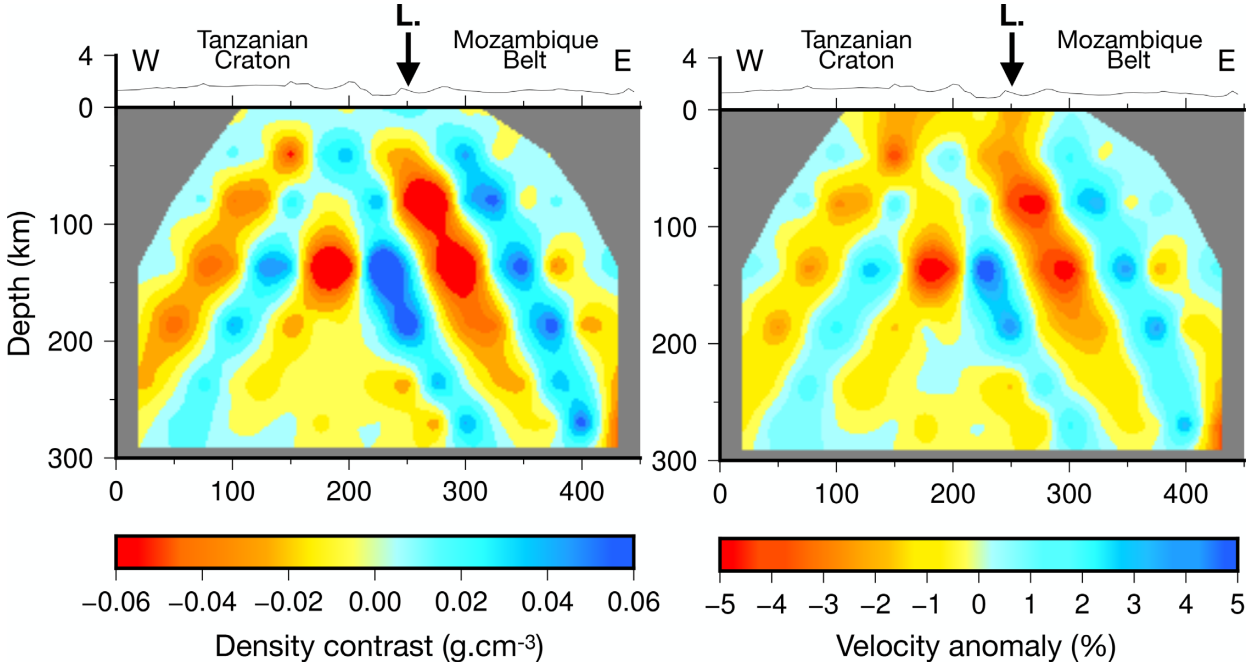


Figure 9. Density and velocity cross-sections for the checkerboard test with ±5 per cent anomalies in layer 4 (135 km depth). The profile is EW oriented at –2.8 latitude.

5.2 Temperature, melt, hydration and composition

Most of the interpretations of the mantle velocity anomaly beneath the East African Rift are only performed in terms of temperature variations, coherent with moderate velocity variations in large-scale tomographic studies below 100 km depth (Huerta *et al.* 2009; Mulibo & Nyblade 2013; Civiero *et al.* 2016). A temperature increase of 100°C can results in a decrease of 0.5-2 per cent in P-wave velocity (Goes *et al.* 2000). Our moderate velocity variations for depths greater than 180 km can be explained by thermal effect only. We propose here that the higher amplitude of the central negative anomaly we image between 40 and 180 km is too strong to be caused only by a temperature effect. If seismic velocities are strongly sensitive to temperature, the density is more sensitive to other parameters, and melt, hydration and composition modification also impact the variations we observed in both parameters (Adams *et al.* 2012). Additional support for thermal and melt contributions to velocity and density variations comes from the sharp edges of the negative central anomaly we image from 80 down to 150 km depth, that coincides with the neighbouring craton and Mobile Belt

Downloaded from https://academic.oup.com/gji/article-abstract/216/3/1693/5237708 by guest on 04 January 2019

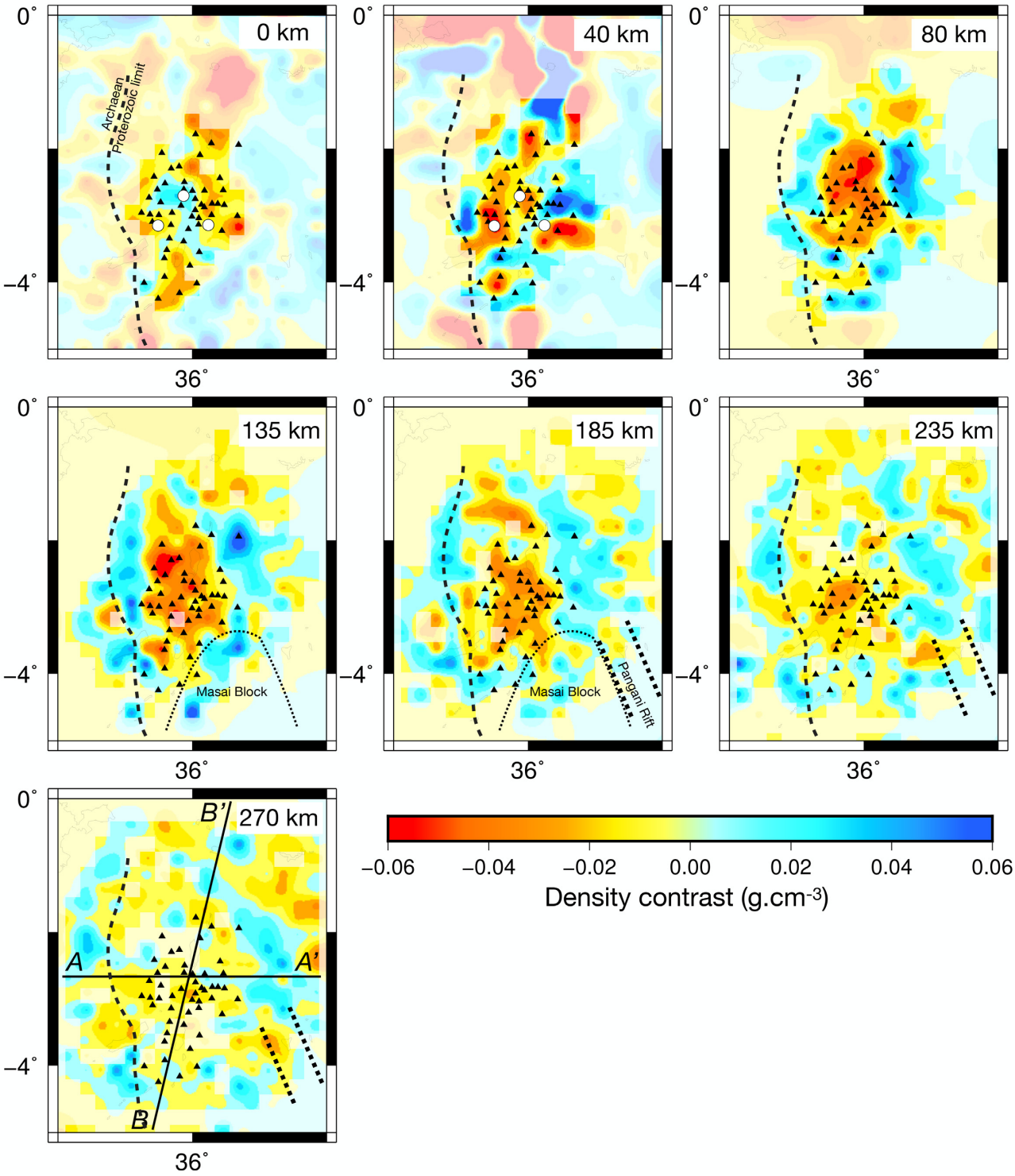


Figure 10. Density contrasts from the joint inversion. The transparency mask indicates zones not constrained by seismic rays. Profiles AA' and BB' for cross-sections are indicated on the last slice. The main volcanic edifices are indicated with white circles in the crustal layers (Lengai, Ngorongoro, Monduli). The presumed Tanzanian Craton, Masai block and Pangani limits are delimited with dotted lines as indicatory.

limits. We interpret the cause of this feature as a combination of compositional, lateral thickness variations and inherited fabrics.

The depleted nature of the mantle may contribute to the highly contrasted velocity/density imaged between the Pan-African orogen and the adjacent Archaean mantle beneath Tanzania (Ritsema *et al.* 1998; Weeraratne *et al.* 2003). Tomographic images of other Archaean cratons surrounded by younger mantle lithosphere delineate smaller velocity contrasts, presuming that melt is a good candidate

Downloaded from https://academic.oup.com/gji/article-abstract/216/3/1693/5237708 by guest on 04 January 2019

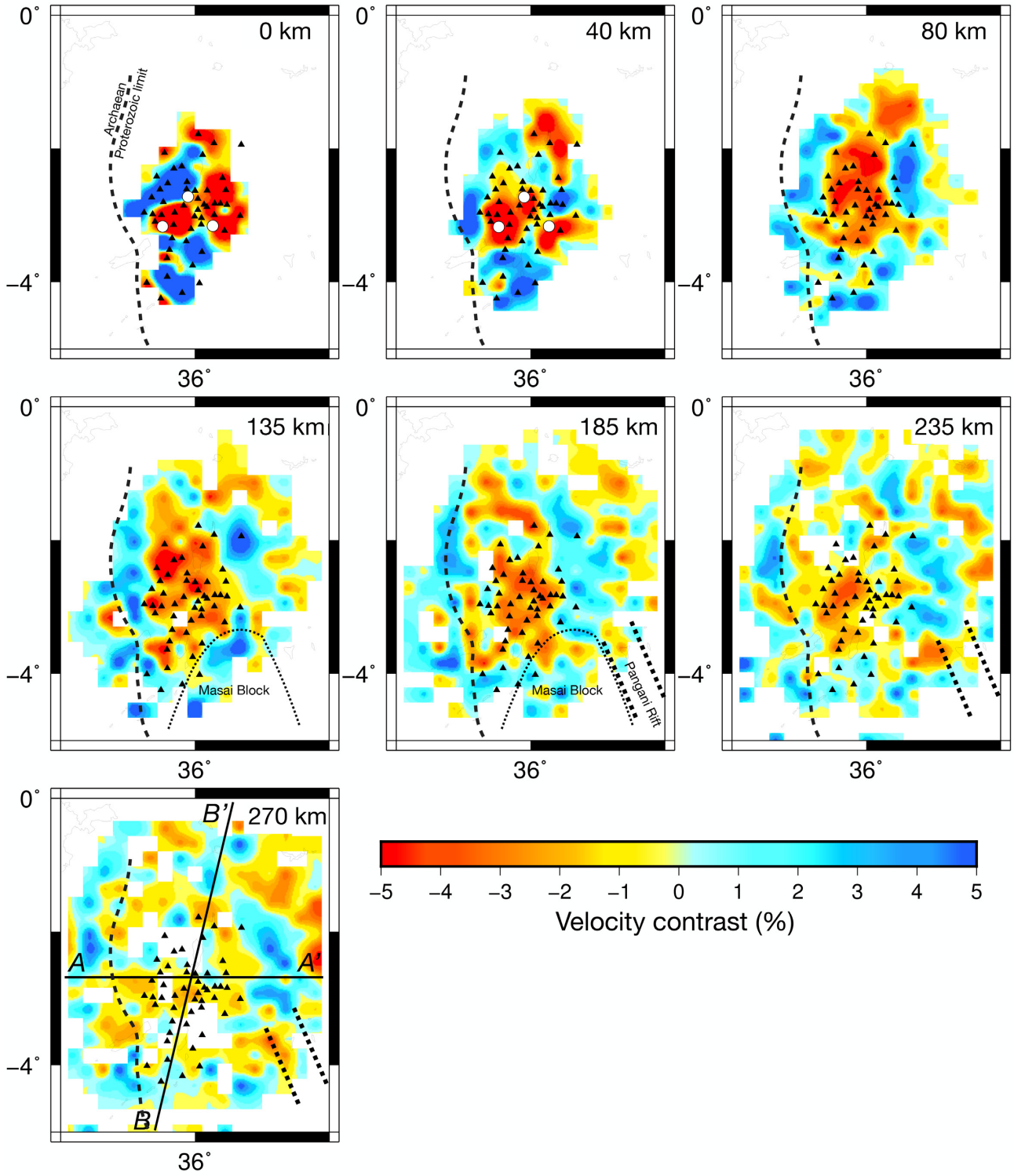


Figure 11. Velocity anomalies from the joint inversion for the seven layers of the model. Profiles AA' and BB' for cross-sections are indicated on the last slice. The main volcanic edifices are indicated with white circles in the crustal layers (Lengai, Ngorongoro, Monduli). The presumed Tanzanian Craton, Masai block and Pangani limits are delimited with dotted lines as indicatory.

to increase the velocity and density contrast observed in the NTD region (Bastow *et al.* 2005; Begg *et al.* 2009,e.g.). Melt has already been proposed to participate with temperature increase to the low velocity low density feature beneath Kenya rift (Green *et al.* 1991; Achauer & the KRISP Teleseismic Working Group 1994; Achauer & Masson 2002). With similar velocity and density variations (ca. -4 per cent in velocity and -0.05 g.cm^{-3} in density between 80 and 135 km), Ravat *et al.* (1999) predicted a temperature rise of ca. 200°C and partial melt content up to 2.5 per cent. With ongoing seismicity, gas emissions, eruptions and intrusions pointing out the

Downloaded from https://academic.oup.com/gji/article-abstract/216/3/1693/5237708 by guest on 04 January 2019

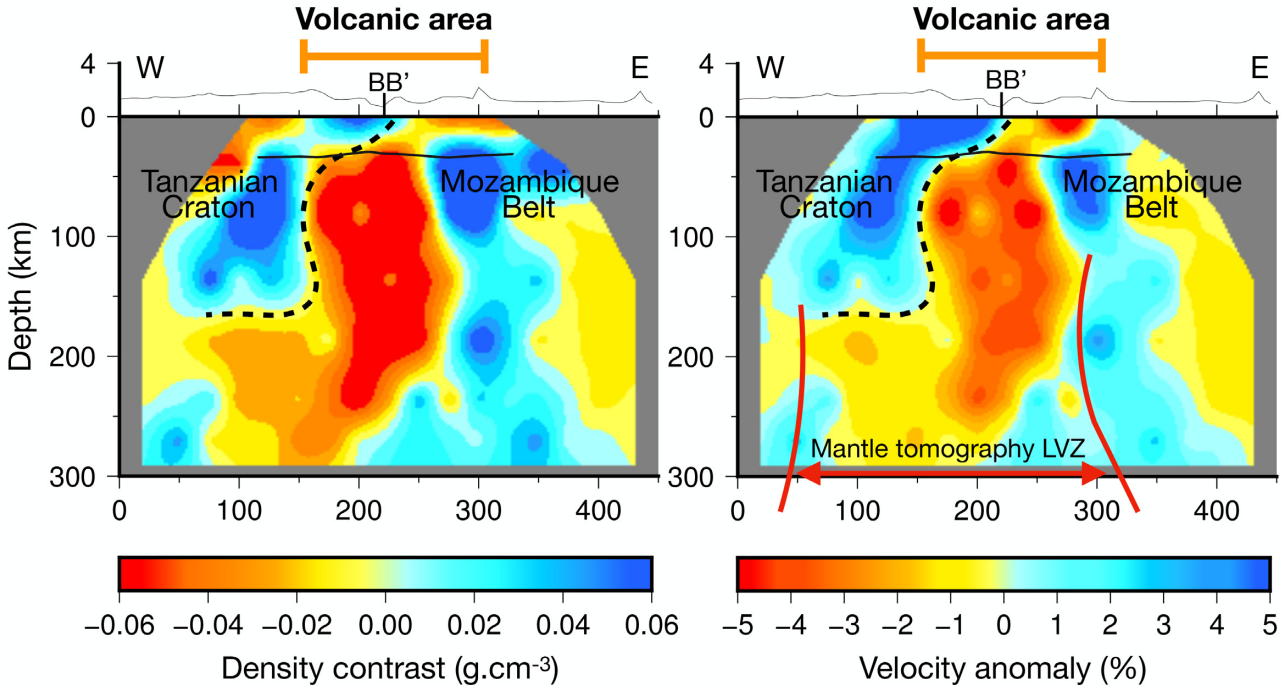


Figure 12. East–west cross-section through the density (left-hand panel) and velocity (right-hand panel) models output from the joint inversion. The profile runs along the AA' line in Fig. 10 at 2.7°S latitude. The upper panel shows the topography (vertical exageration) with the volcanic area of the North Tanzanian Divergence (NTD) and the junction with the BB' profile. On the bottom panel, dashed black line displays the interpreted Tanzanian Craton edge on the cross-section. Approximative low velocity zone (LVZ) boundary from mantle tomography of (Mulibo & Nyblade 2013) is marked in thick red line for information. Moho variation from receiver function is emphasized by the continuous black line in the first 50 km (Plasman *et al.* 2017).

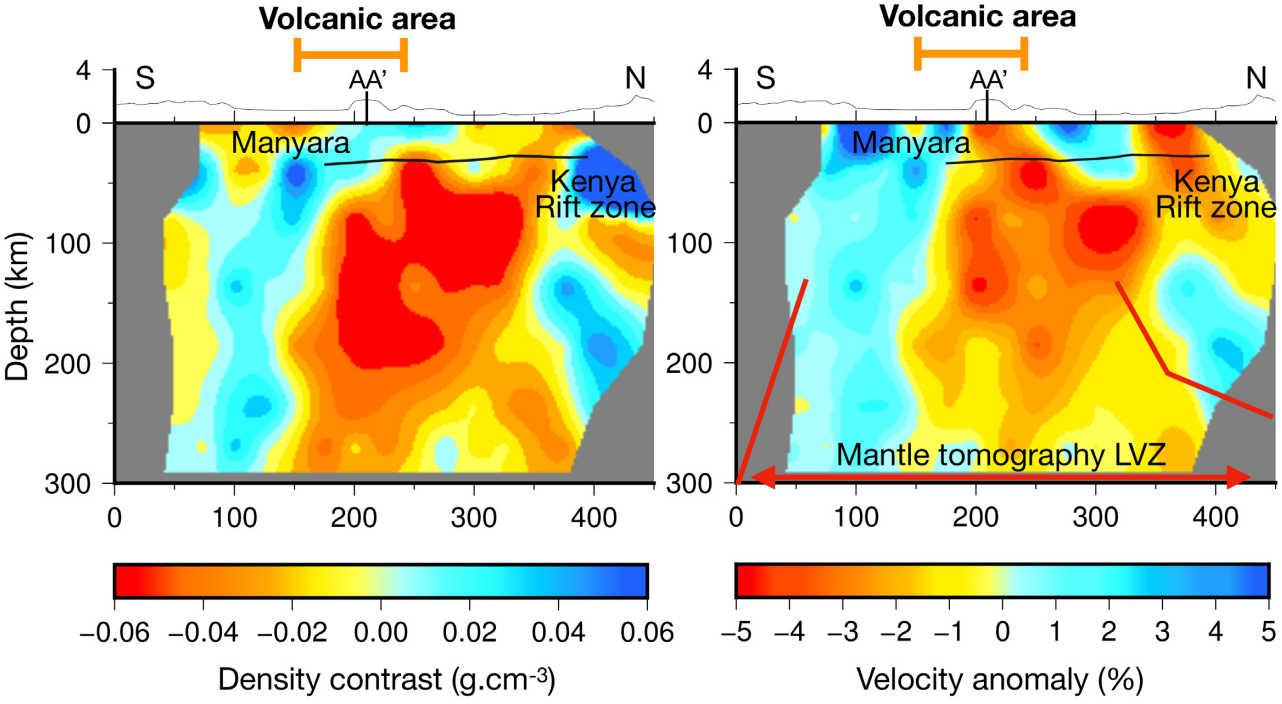


Figure 13. North–south cross-section through the density (left-hand panel) and velocity (right-hand panel) models output from the joint inversion. The profile runs along the BB' line in Fig. 10. The upper panel shows the topography (vertical exageration) with the volcanic area of the North Tanzanian Divergence (NTD) and the junction with the AA' profile. On the bottom panel, Manyara and Kenya rift location are indicated. Approximative low velocity zone (LVZ) boundary from mantle tomography of (Mulibo & Nyblade 2013) is marked in thick red line for information. Moho variation from receiver function is emphasized by the continuous black line in the first 50 km (Plasman *et al.* 2017).

Downloaded from https://academic.oup.com/gji/article-abstract/216/3/1693/5237708 by guest on 04 January 2019

presence of fluids within the crust (Plasman *et al.* 2017; Roecker *et al.* 2017), melt is undoubtedly present within the MNM rift zone. Previous petrological studies in this area shows that the melt fraction should be greater beneath the rift axis than beneath its flanks, coherent with the decrease of density and velocity signal sideways (Latin *et al.* 1993; Foley & Fischer 2017). P-wave velocity can be reduced by 2 per cent to 9 per cent within the lithosphere (70-150 km) for melt fraction between 1 per cent to 5 per cent (Ravat *et al.* 1999; Goes *et al.* 2000; Clark & Lesher 2017). The amount of velocity reduction also depends on melt geometry, shape and pressure (e.g. Mainprice 1997; Takei 2002; Clark & Lesher 2017). These values represent an upper bound limit as melt is not the only parameter altering velocity and density values. Besides, taking into account the partial recovery of amplitude in our models (smearing effect, smoothing factor, ...), we estimate that 2 per cent or 3 per cent is the maximum percentage of melt present in the upper mantle beneath the MNM Branch.

The Tanzanian Craton and Pan-African Mobile Belt are both associated with high density and velocity bodies, as reported in most of the mantle tomographic studies in the region (e.g. Ritsema *et al.* 1998; O'Donnell *et al.* 2013). The Mobile Belt clearly exhibits the highest positive contrast in our models (Fig. 12), where previous magnetotelluric studies also reveal high resistivity within the lithosphere (Selway 2015). We interpret this feature in terms of hydrogen content variation, as an hydrogen enrichment will decrease the density, velocity and resistivity signal (e.g. Karato 1990, 1995; Mavko *et al.* 2009). The Tanzanian Craton appears then more hydrous than the Mobile Belt. Enriched hydrogen content is classically related to the reduction of plate strength and is often used to explain the location of lithospheric deformation and rift propagation (Kushiro *et al.* 1968; Peslier *et al.* 2010). This however contradicts the fact that the MNM rift arm has preferentially developed within the less hydrous Pan-African lithosphere (Fig. 1). Our results then reinforce the idea that high hydrogen content does not systematically reduce plate strength as first thought. Alternatively, localized shear zones with reduced grain size by earlier deformation and localized fluid migration at the craton boundary may make the mobile belt a better candidate for rifting location (Tommasi & Vauchez 2001; Selway 2015). It emphasizes the role of composition and inherited structures in the localisation of the deformation in the Eastern Branch of the rift.

5.3 Geodynamic implications

Present-day topography, gravity anomalies, magmatism and surface uplift observed in East Africa has been previously related to the interaction of asthenospheric upwelling with continental lithosphere (e.g. Ebinger & Sleep 1998; Fishwick & Bastow 2011). Yet in the MNM rift zone, the role of a thick cratonic lithosphere overlying Archaean mantle in the localization of the strain and the magmatism distribution remains an outstanding question (e.g. King & Ritsema 2000; Priestley *et al.* 2008; Albaric *et al.* 2014; Currie & van Wijk 2016). Based on thermal modelling (Priestley & McKenzie 2006) and shear wave tomographic models (Fishwick 2010), the lithospheric thickness variation has been estimated beneath African continent at a regional scale and clearly shows a thinning beneath the Eastern rift in Tanzania (Priestley *et al.* 2008; Fishwick 2010). Temporal, spatial and compositional analyses of different eruptive rocks in the Eastern Branch of the EAR also support the concept of a convecting asthenospheric upwelling and a lithospheric thinning in Kenya and North Tanzania, with decreasing depths of origin of magma with time (Wendlandt & Morgan 1982; Latin *et al.* 1993; Foley & Fischer 2017). Two difficulties arise in our case to estimate spatial variations in the 1300°C isotherm, and hence lithospheric thickness variations beneath the MNM rift zone. First, the use of relative delay times in our methodology rules out the estimate of an absolute seismic velocity. Second, thermal modification of the lithosphere is not the only factor to cause variations in velocity and density we observed, as demonstrated above. We can hardly propose a constrained lithospheric thickness beneath the MNM rift arm based on our velocity density contrasts alone. We can, however, use the crustal stretching estimate of 20-30 per cent made by Plasman *et al.* (2017) beneath the Natron Basin as a minimum bound for the amount of lithospheric thinning that has occurred since rift onset. This would translate to about 60 km of mantle lithospheric thinning, assuming that an initial 200 km thick Archaean lithosphere underlay the MNM rift prior to rifting. A resulting lithospheric thickness of 140 km beneath the MNM is coherent with the xenoliths analysis in this area (Vauchez *et al.* 2005; Baptiste *et al.* 2015). It means that the MNM rift Branch could be considered as a less mature and evolved stage compared with the Main Ethiopian Rift (MER), where the mantle lithosphere was fundamentally altered and thermally thinned by a plume head impingement prior to rifting (e.g. Ayalew & Gibson 2009). The Main Ethiopian Rift presents an older (∼18 Ma, e.g. Ebinger *et al.* (1993)) and higher stretching history (70 per cent, e.g. Dugda *et al.* (2007)) as well as thick underplating layers (e.g. Mackenzie *et al.* 2005). However, the crucial contributions of composition, structural and thermal variations which seem to drive the MNM rift evolution can't be directly transposed to the Main Ethiopian Rift, even if previous interpretations in this more evolved branch have suggested the influence of lithospheric structural inheritances (Bastow *et al.* 2008, 2011).

Our results further demonstrate the clear interaction between mantle upwelling and inherited fabrics like the Tanzanian Craton and the Mobile Belt. The contact between the craton and the MNM rift zone signature is overall west dipping in all broader mantle tomographic studies for depths deeper than 100 km (Ritsema *et al.* 1998; O'Donnell *et al.* 2013; Mulibo & Nyblade 2013). This leads some researchers to propose a unique deep mantle super plume that impinges the craton and circumvent it to create opening and divergence at the cratonic edge (e.g. Huerta *et al.* 2009; Koptev *et al.* 2016). However, our models, for the first time, reveal the sub-vertical geometry of the craton-orogenic belt boundary for the uppermost 150 km, where the lateral resolution for our inversion is the best. The extreme narrowness of the central negative anomaly beneath the MNM rift Branch clearly indicates that its lateral extension is limited by the inherited lithospheric fabrics like cratonic keel and mobile belt. The geometry of the anomaly is very similar to what is imaged beneath the Rio Grande rift (Gao *et al.* 2004; West *et al.* 2004). We infer from these observations that thermal erosion and lithospheric thinning are present and active beneath the MNM rift Branch. Asthenospheric upwelling may be reinforced by small-scale convection caused by compositional variations and lithospheric step between cratonic edges and neighbouring units (van Wijk *et al.* 2008). To maintain the craton root stability, though, its hydration should track only modern metasomatism and cratonic root removal (Currie & van Wijk 2016). The small Tanzanian Craton is thinner than the Kaapvaal and Congo Cratons, and kimberlite compositions show progressive thinning and hydration (e.g. Vauchez *et al.* 2005). This is consistent with progressive lateral erosion over time (Sleep *et al.* 2002; Currie & van Wijk 2016). Local lateral changes in composition may also help to preserve cratonic roots and control the mantle upwelling extension towards the surface. It can be the

Downloaded from https://academic.oup.com/gji/article-abstract/216/3/1693/5237708 by guest on 04 January 2019

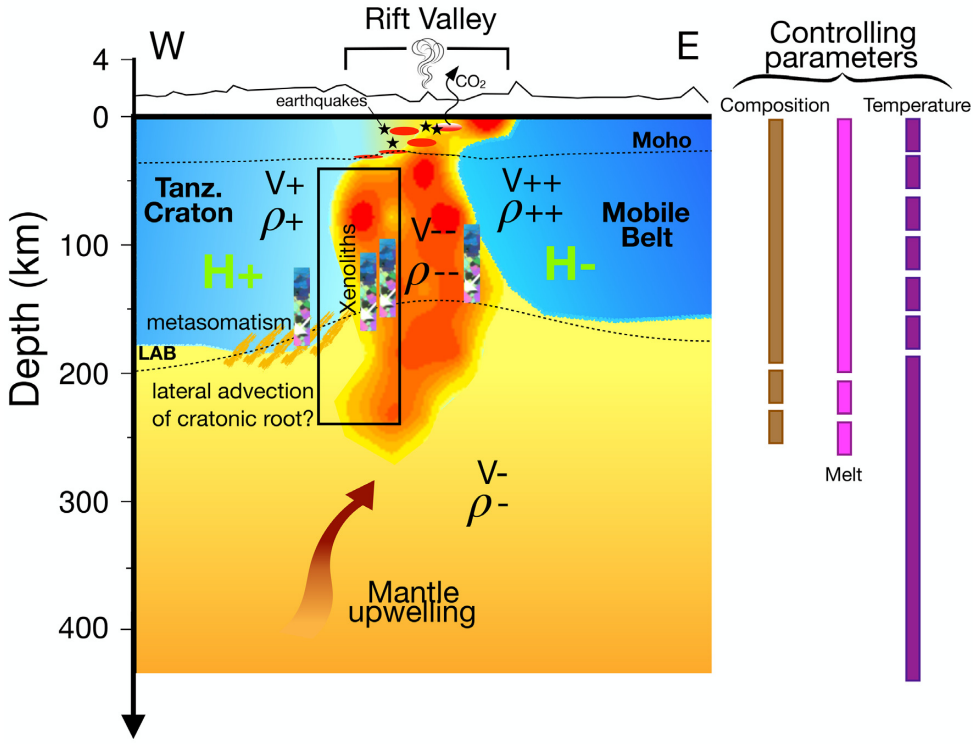


Figure 14. Interpretative scheme for upper mantle processes involved in the Eastern Branch of the East African Rift. The regional mantle upwelling observed in large scale tomographic studies correspond to 1 or 2 per cent of seismic velocity decrease (e.g. Ritsema *et al.* 1998), whereas composition variation and melt presence both supplement the rift centred negative signature above 200 km. Lithospheric thinning can reach 60 km for an initially 200 km thick lithosphere (LAB: Lithosphere Asthenosphere Boundary) consistent with the xenolith signature within the rift axis and near the craton margin (coloured rectangle boxes, Vauchez *et al.* 2005; Baptiste *et al.* 2015). The hydrated nature of the Tanzanian Craton (H+) is compatible with lateral advection of cratonic root and a metasomatized mantle (black frame), as indicated through geophysical observations (Selway 2015) and petrophysics analyses (Rudnick *et al.* 1993; Vauchez *et al.* 2005). The crust though moderately stretched is consequently modified with melt inclusions (Roecker *et al.* 2017), underplating (Plasman *et al.* 2017), CO_2 degasing (Lee *et al.* 2016) and brittle deformation (Weinstein *et al.* 2017).

case for the Manyara rift Branch, where we interpret the diverging density and velocity signature within the crust as the transition from Pan-African to Archaean units favouring the rift propagation. The Masai cratonic block limits the eastern extension of mantle upwelling within the lithosphere.

6 CONCLUSION

We combine gravity and P-wave travel times from a two year-long experiment to obtain density and velocity variations from the surface down to ca. 270 km beneath the North Tanzanian Divergence. Our results are dominated by a clear and strong low density low velocity anomaly restricted to the MNM rift Branch. We propose that this anomaly is connected to the broad mantle LVZ imaged in global tomographic studies. Its stronger amplitude in the lithosphere reflects melt, hydration and composition variations in addition to thermal effect, due to the interaction between a mantle upwelling and the highly heterogeneous thick cratonic lithosphere of the Eastern Branch of the East African Rift (Fig. 14).

We estimate that 2–3 per cent of melt is necessary to complete the thermal effect of a mantle upwelling in our models. First restricted to the main magmatic centres within the crust, the location of melt is widening with depth to concern the whole MNM rift Branch at 150 km depth (Fig. 14).

Additional lateral changes of composition locally create even more contrasted anomaly within the first 100 km. They are also required to explain the sharp and rather vertical boundaries of the central low velocity low density anomaly beneath the MNM rift zone, as well as the stability of the cratonic root. The Masai block is separated from the Tanzanian Craton by a crustal terrane that exhibits a counter density velocity signature we interpret as a change in composition controlling the propagation of the deformation (seismicity and magmatism distribution) as well as the melt extent south of Manyara. The presence of Archaean and Proterozoic units imaged by strong positive bodies drives the lithospheric low velocity low density zone, and restricts its lateral extension within the MNM zone. Southeastward propagation of asthenospheric low velocity low density material beneath Pangani rift arm is possible but confined below 200 km depth.XXX

Our results support the idea of a 3-D distribution of the crust and mantle lithospheric stretching, which was probably enhanced by lateral compositional and hydration variations at the craton-orogenic belt boundary. Combined with the inherited structural fabrics, this lateral heterogeneity appears to have guided strain and magmatism localisation at the onset of rifting in this sector of the Eastern rift.

ACKNOWLEDGEMENTS

We thank three anonymous reviewers and the editor for their constructive remarks. The seismic instruments were provided by the Incorporated Research Institutions for Seismology (IRIS) through the PASSCAL Instrument Centre at New Mexico Tech. Data collected will be available through the IRIS Data Management Centre. The facilities of the IRIS Consortium are supported by the National

Downloaded from https://academic.oup.com/gji/article-abstract/216/3/1693/5237708 by guest on 04 January 2019

Science Foundation under Cooperative Agreement EAR-1261681 and the DOE National Nuclear Security Administration. We deeply thank the university of Nantes (Antoine Mocquet, E. Beucler) and Brest for the loan of 10 OSIRIS dataloggers and Neomax sensors. Gravity data were acquired thanks to INSU-GMOB facilites. We are very grateful for the assistance of RPI graduate student Anastasia Rodzianko, Rochester undergraduate students Eli Witkin, Catherine Lambert, Avery Palardy and Geosciences Montpellier graduate student Nathalie Rasendra in seismic installations and servicing. Nicolas Le Moigne, Cédric Champollion, Erik Doerflinger, Majura Songo have collected the 178 new gravity points in Manyara and Natron area. We thank Yoann Douillas and Clément Dubois for their help in picking the P-waves arrival time during their undergraduate internship. Work was conducted with approval by the Commission for Science and Technology (COSTECH, Tanzania) and the National Council for Science and Technology (Kenya). We are grateful for logistical support from Tanzania National Parks Commission and to the Ngorongoro National Park. We could not have achieved this work without logistical assistance from primary and secondary school teachers throughout the region, the Masai clans in Kenya and Tanzania, driver-guides from Fortes Tours, the Ngorongoro conservation area, Tanapa and the French Ambassy. Finally, we want to thank Majura Songo and Sindato Moreto and all the people from CoLiBrEA (ANR-12-JS06-0004) and Crafti (EAR-1261681) projects.

REFERENCES

Achauer, U. & Masson, F., 2002. Seismic tomography of continental rifts revisited: from relative to absolute heterogeneities, *Tectonophysics,* **358,** 17–37.

Achauer, U., the KRISP Teleseismic Working Group, 1994. New ideas on the Kenya rift based on the inversion of the combined dataset of the 1985 and 1989/90 seismic tomography experiments, *Tectonophysics,* **236,** 305–329.

Adams, A., Nyblade, A. & Weeraratne, D., 2012. Upper mantle shear wave velocity structure beneath the East African plateau: evidence for a deep, plateau wide low velocity anomaly, *Geophys. J. Int.,* **189**(1), 123–932.

Albaric, J. *et al.*, 2010. Contrasted seismogenic and rheological behaviours from shallow and deep earthquake sequences in the North Tanzanian Divergence, East Africa, *J. Afr. Earth Sci.,* **58**(5), 799–811.

Albaric, J., Déverchère, J., Perrot, J., Jakovlev, A. & Deschamps, A., 2014. Deep crustal earthquakes in North Tanzania, East Africa: interplay between tectonic and magmatic processes in an incipient rift, *Geochem. Geophys. Geosyst.,* **15**(2), 374–394.

Aulbach, S., Rudnick, R. & McDonough, W., 2008. Lithospheric mantle sources within the East African Rift, Tanzania, *Geochem. Geophys. Geosyst.,* **15**(2), 374–394.

Ayalew, D. & Gibson, S., 2009. Head-to-tail transition of the Afar mantle plume: geochemical evidence from a Miocene bimodal basalt-rhyolite succession in the Ethiopian Large Igneous Province, *Lithos,* **112,** 461–476.

Baer, G., Hamiel, Y., Shamir, G. & Nof, R., 2008. Evolution of a magma-driven earthquake swarm and triggering of the nearby Oldoinyo Lengai eruption, as resolved by InSAR, ground observations and elastic modeling, east african rift, 2007, *Earth planet. Sci. Lett.,* **272**(1), 339–352.

Baptiste, V., Tommasi, A., Vauchez, A., Demouchy, S. & Rudnick, R., 2015. Deformation, hydration, and anisotropy of the lithospheric mantle in an active rift: Constraints from mantle xenoliths from the North Tanzanian Divergence of the East African Rift, *Tectonophysics,* **639,** 34–55.

Bastow, I. & Keir, D., 2011. The protracted development of the continento-cean transition in Afar, *Nat. Geosci.,* **4,** 248–250.

Bastow, I., Stuart, G., Kendall, J.-M. & Ebinger, C., 2005. Upper-mantle seismic structure in a region of incipient continental breakup: northern Ethiopian rift, *Geophys. J. Int.,* **162**(2), 479–493.

Bastow, I., Keir, D. & Daly, E., 2011. The Ethiopia Afar Geoscientific Lithospheric Experiment (EAGLE): probing the transition from continental rifting to incipient seafloor spreading, *Geol. Soc. Am. Spec. Paper,* **478,** 51–76.

Bastow, I.D., Nyblade, A.A., Stuart, G.W., Rooney, T.O. & Benoit, M.H., 2008. Upper mantle seismic structure beneath the Ethiopian hot spot: rifting at the edge of the African low-velocity anomaly, *Geochem. Geophys. Geosyst.,* **9**(12), Q12022.

Baudouin, C., Parat, F., Denis, C. & Mangasini, F., 2016. Nephelinites lavas at early stage of rift initiation (Hanang volcano, North Tanzanian Divergence), *Contrib. Mine. Petro.,* **171**(7), 64.

Begg, G. *et al.*, 2009. The lithospheric architecture of Africa: seismic tomography, mantle petrology, and tectonic evolution, *Geosphere,* **5**(1), 23.

Benoit, M.H., Nyblade, A.A., Owens, T.J. & Stuart, G., 2006. Mantle transition zone structure and upper mantle S velocity variations beneath Ethiopia: evidence for a broad, deep-seated thermal anomaly, *Geochem. Geophys. Geosyst.,* **7,** Q11013.

Biggs, J., Amelung, F., Gourmelen, N., Dixon, T. & Kim, S.-W., 2009. InSAR observations of 2007 Tanzania rifting episode reveal mixed fault and dyke extension in an immature continental rift, *Geophys. J. Int.,* **179,** 549–558.

Birch, F., 1961. The velocity of compressional waves in rocks to 10 kilobars, *J. geophys. Res.,* **66,** 2199–2224.

Birt, C.S., Maguire, P. K.H., Khan, M.A., Thybo, H. & Keller, G.R.J.P., 1997. The influence of pre-existing structures on the evolution of the southern Kenya Rift Valley-evidence from seismic and gravity studies, *Tectonophysics,* **278**(1), 211–242.

Calais, E. *et al.*, 2008. Strain accommodation by slow slip and dyking in a youthful continental rift, East Africa, *Nature,* **456,** 783–787.

Christensen, N.I. & Mooney, W.D., 1995. Seismic velocity structure and composition of the continental crust: a global view., *J. geophys. Res.,* **100,** 9761–9785.

Chung, D., 1972. Birch's law: why is it so good? *Science,* **177,** 261–263.

Civiero, C. *et al.*, 2016. Small-scale thermal upwellings under the northern East African Rift from S travel time tomography, *J. geophys. Res.: Solid Earth,* **121**(10), 7395–7408.

Clark, A. & Lesher, C., 2017. Elastic properties of silicate melts: implications for low velocity zones at the lithosphere-asthenosphere boundary, *Sci. Adv.,* **3,** e1701312.

Currie, C.A. & van Wijk, J., 2016. How craton margins are preserved: Insights from geodynamic models, *J. Geodyn.,* **100,** 144–158.

Dawson, J., 1992. Neogene tectonics and volcanicity in the North Tanzania sector of the Gregory Rift Valley: contrasts with the Kenya sector, *Tectonophysics,* **204,** 81–92.

Dugda, M.T., Nyblade, A.A. & Julia, J., 2007. Thin lithosphere beneath the Ethiopian plateau revealed by a joint inversion of Rayleigh wave group velocities and receiver functions, *J. geophys. Res.: Solid Earth,* **112**(B8).

Dziewonski, A.M. & Anderson, D.L., 1981. Preliminary reference Earth model, *Phys. Earth planet. Int.,* **25,** 297–356.

Ebinger, C., Yemane, J. T., WoldeGabriel, G., L.Aronson, J. & Walter, R.C., 1993. Late Eocene-recent volcanism and faulting in the southernmain Ethiopian rift, *J. Geol. Soc. Lond.,* **150,** 99–108.

Ebinger, C., Poudjom-Djomani, Y., Mbede, E. & Foster, A., 1997. Rifting Archaean lithosphere: the Eyasi-Manyara-Natron rifts, East Africa, *J. Geol. Soc. Lond.,* **154**(6), 947–960.

Ebinger, C.J. & Sleep, N.H., 1998. Cenozoic magmatism throughout east Africa resulting from impact of a single plume, *Nature,* **395,** 788–791.

Evans, J. & Achauer, U., 1993. Teleseismic velocity tomography using the ACH method: theory and application to continental scale, in *Seismic tomography: Theory and Practice,* pp. 319–360, Chapman and Hall.

Fishwick, S., 2010. Surface wave tomography: imaging of the lithosphere-asthenosphere boundary beneath central and southern Africa? *Lithos,* **120,** 63–73.

Fishwick, S. & Bastow, I.D., 2011. Towards a better understanding of African topography: a review of passive-source seismic studies of the African crust and upper mantle, *Geol. Soc., Lond., Spec. Publicat.,* **357**(1), 343–371.

Foley, F. & Fischer, T., 2017. An essential role for continental rifts and lithosphere in the deep carbon cycle, *Nat. Geosci.,* **10,** 897–902.

Downloaded from https://academic.oup.com/gji/article-abstract/216/3/1693/5237708 by guest on 04 January 2019

Foster, A., Ebinger, C. & Mbede, E. D.R., 1997. Tectonic development of the northern Tanzania sector of the East African rift system, *J. Geol. Soc. Lond.,* **154,** 689–700.

French, S. & Romanowicz, B., 2015. Broad plumes rooted at the base of the Earth's mantle beneath major hotspots, *Nature,* **525,** 95–99.

Gao, W., Grand, S.P., Baldridge, W., Wilson, D., West, M. & Ni, J.F.a.R., 2004. Upper mantle convection beneath the central Rio Grande rift imaged by P and S wave tomography, *J. geophys. Res.,* **109**(B03305).

Garnero, E., McNamara, A. & Shim, S.-H., 2016. Continent-sized anomalous zones with low seismic velocity at the base of Earth's mantle, *Nat. Geosci.,* **9,** 481–489.

Gautier, S., Latorre, D., Virieux, J., Deschamps, A., Skarpelos, C., Sotiriou, A., Serpetsidaki, A. & Tselentis, A., 2006. A new passive tomography of the Aigion area (Gulf of Corinth, Greece) from the 2002 data set, *Pure appl. Geophys.,* **163**(2), 431–453.

Goes, S., Govers, R. & Vacher, P., 2000. Shallow mantle temperatures under Europe from P and S wave tomography, *J. geophys. Res.,* **105**(B5), 11 153–11 169.

Green, W., Achauer, U. R. &M., 1991. A 3-dimensional seismic image of the crust and upper mantle beneath the Kenya rift, *Nature,* **354,** 199–203.

Hansen, S.E., Nyblade, A.A. & Benoit, M.H., 2012. Mantle structure beneath Africa and Arabia from adaptively parameterized P-wave tomography: implications for the origin of Cenozoic Afro-Arabian tectonism, *Earth planet. Sci. Lett.,* **319-320,** 23–34.

Huerta, A.D., Nyblade, A.A. & Reusch, A.M., 2009. Mantle transition zone structure beneath Kenya and Tanzania: more evidence for a deep-seated thermal upwelling in the mantle, *J. geophys. Int.,* **177**(3), 1249–1255.

Hui, H., Peslier, A., Rudnick, R., Simonetti, A. & Neal, C., 2015. Plume-cratonic lithosphere interaction recorded by water and other trace elements in peridotite xenoliths from the Labait volcano, Tanzania, *Geochem. Geophys. Geosys.,* **16,** 1687–1710.

Julià, J., Ammon, C. & Nyblade, A., 2005. Evidence for mafic lower crust in Tanzania, East Africa, from joint inversion of receiver functions and Rayleigh wave dispersion velocities, *Geophys. J. Int.,* **162,** 555–569.

Karato, S., 1990. The role of hydrogen in the electrical conductivity of the upper mantle, *Nature,* **347,** 272–273.

Karato, S., 1995. Effect of water on seismic wave velocities in the upper mantle, *Proc. Japan Acad.,* **71**(B), 61–66.

Kennett, B. & Engdahl, E., 1991. Traveltimes for global earthquake location and phase identification, *Geophys. J. Int.,* **105,** 429–465.

King, S.D. & Ritsema, J., 2000. African hot spot volcanism: small-scale convection in the upper mantle beneath cratons, *Science,* **290**(5494), 1137–1140.

Koptev, A., Burov, E., Calais, E., Leroy, S., Gerya, T., Guillou-Frottier, L. & Cloetingh, S., 2016. Contrasted continental rifting via plume-craton interaction: applications to central east African rift, *Geosci. Front.,* **7**(2), 221–236.

Kushiro, I., Syono, Y. & Akimoto, S.-I., 1968. Melting of a peridotite nodule at high pressures and high water pressures, *J. geophys. Res.,* **73**(18), 6023–6029.

Latin, D., Norry, M. & Tarzey, R., 1993. Magmatism in the Gregory rift, East Africa: evidence for melt generation by a plume, *J. Petrol.,* **34,** 1007–1027.

Le Gall, B., Nonnotte, P., Rolet, J., Benoit, M., Guillou, H., Mousseau-Nonnotte, M., Albaric, J. & Déverchère, J., 2008. Rift propagation at craton margin: distribution of faulting and volcanism in the North Tanzanian Divergence (East Africa) during Neogene times, *Tectonophysics,* **448**(1), 1–19.

Lee, H., Muirhead, J., Fischer, T., Ebinger, C., Kattenhorn, S., Sharp, Z. & Kianji, G., 2016. Massive and prolonged deep carbon emissions associated with continental rifting, *Nat. Geosci.,* **9**(2), 145–149.

Lindenfeld, M. & Rümpker, G., 2011. Detection of mantle earthquakes beneath the East African Rift, *Geophys. J. Int.,* **186**(1), 1–5.

Mackenzie, G.D., Thybo, H. & Maguire, P. K.H., 2005. Crustal velocity structure across the Main Ethiopian Rift: results from two-dimensional wide-angle seismic modelling, *Geophys. J. Int.,* **162,** 994–1006.

Mainprice, D., 1997. Modelling the anisotropic seismic properties of partially molten rocks found at mid-ocean ridges, *Tectonophys.,* **279,** 161–179.

Mana, S., Furman, T., Turrin, B., Feigenson, M. & Swisher, C., 2015. Magmatic activity across the East African North Tanzanian Divergence Zone, *J. Geol. Soc.,* **172,** 368–389.

Mavko, G., Mukerji, T. & Dvorkin, J. 2009. *The Rock Physics Handbook: Tools for Seismic Analysis of Porous Media,* 2nd edn, Cambridge Univ. Press.

McHenry, L.J., Luque, L., Gomez, J.A. & Diez-Martin, F., 2011. Promise and pitfalls for characterizing and correlating the zeolitically altered tephra of the Pleistocene Peninj group, Tanzania, *Quat. Res.,* **75**(3), 708–720.

Muirhead, J.D., Kattenhorn, S.A. & Le Corvec, N., 2015. Varying styles of magmatic strain accommodation across the East African Rift, *Geochem. Geophys. Geosyst.,* **16**(8), 2775–2795.

Mulibo, G.D. & Nyblade, A.A., 2013. The P and S wave velocity structure of the mantle beneath eastern Africa and the African superplume anomaly, *Geochem. Geophys. Geosyst.,* **14**(8), 2696–2715.

Mulibo, G.D. & Nyblade, A.A., 2013b. Mantle transition zone thinning beneath eastern Africa: Evidence for a whole-mantle superplume structure, *Geophys. Res. Lett.,* **40**(14), 3562–3566.

Mulibo, G.D. & Nyblade, A.A., 2016. The seismotectonics of southeastern Tanzania: Implications for the propagation of the eastern branch of the East African Rift, *Tectonophys.,* **674,** 20–30.

Nonnotte, P., Guillou, H., Le Gall, B., Benoit, M., Cotten, J. & Scaillet, S., 2008. New K-Ar age determinations of Kilimanjaro volcano in the north Tanzanian diverging rift, East Africa, *J. Volc. Geotherm. Res.,* **173**(1–2), 99–112.

Nyblade, A., Pollack, H., Jones, D., Podmore, F. & Mushayandebvu, M., 1990. Terrestrial heat flow in East and Southern Africa, *J. geophys. Res.,* **95**(B11), 17 371–17 384.

Nyblade, A.,Langston, C.A. Last, R., Birt, C. & Owens, T., 1996. Seismic experiment reveals rifting of craton in Tanzania, in, *EOS, Trans. Am. geophys. Un.,* **77,** 517–521.

O'Donnell, J.-P., Adams, A., Nyblade, A., Mulibo, G. & Tugume, F., 2013. The uppermost mantle shear wave velocity structure of eastern Africa from Rayleigh wave tomography: constraints on the rift evolution, *Geophys. J. Int.,* **194,** 961–978.

Pérez-Gussinyé, M., Metois, M., Fernàndez, M., Vergés, J., Fullea, J. & Lowry, A., 2009. Effective elastic thickness of Africa and its relationship to other proxies for lithospheric structure and surface tectonics, *Earth planet. Sci. Lett.,* **287**(1), 152–167.

Peslier, A.H., Woodland, A. & Bell, D. M.L, 2010. Olivine water contents of the continental lithosphere and the longevity of cratons, *Nature,* **467,** 78–81.

Petit, C. & Ebinger, C., 2000. Flexure and mechanical behavior of cratonic lithosphere: gravity models of the East African and Baikal rifts, *J. geophys. Res.,* **105**(B8), 19 151–19 162.

Pik, R., Marty, B. & Hilton, D.R., 2006. How many mantle plumes in Africa? The geochemical point of view, *Chem. Geol.,* **226**(3-4), 100–114.

Plasman, M. *et al.*, 2017. Lithospheric low-velocity zones associated with a magmatic segment of the Tanzanian rift, East Africa, *Geophys. J. Int.,* **210**(1), 465–481.

Priestley, K. & McKenzie, D., 2006. The thermal structure of the lithosphere from shear wave velocities, *Earth planet. Sci. Lett.,* **244,** 285–301.

Priestley, K., McKenzie, D., Debayle, E. & Pilidou, S., 2008. The African upper mantle and its relationship to tectonics and surface geology, *Geophys. J. Int.,* **175,** 1108–1126.

Ravat, D., Lu, Z. & Braile, L., 1999. Velocity-density relationships and modelling the lithospheric density variations of the Kenya rift, *Tectonophys.,* **302,** 225–240.

Ritsema, J., Nyblade, A.A., Owens, T.J., Langston, C.A. & VanDecar, J.C., 1998. Upper mantle seismic velocity structure beneath Tanzania, east Africa: Implications for the stability of cratonic lithosphere, *J. geophys. Res.: Solid Earth,* **103**(B9), 21201–21213.

Ritsema, J., Heijst, H.J.v. & Woodhouse, J.H., 1999. Complex shear wave velocity structure imaged beneath Africa and Iceland, *Science,* **286**(5446), 1925–1928.

Roecker, S., Thurber, C. & Mcphee, D., 2004. Joint inversion of gravity and arrival time data from Parkfield: new constraints on structure and

Downloaded from https://academic.oup.com/gji/article-abstract/216/3/1693/5237708 by guest on 04 January 2019

hypocenter locations near the SAFOD drill site, *Geophys. Res. Let.,* **31,** L12S04.
Roecker, S. *et al.*, 2017. Subsurface images of the Eastern rift, Africa, from the joint inversion of body waves, surface waves, and gravity: investigating the role of fluids in early-stage continental rifting, *Geophys. J. Int.,* **210,** 931–950.
Rudnick, R.L., McDonough, W.F. & Chappell, B.W., 1993. Carbonatite metasomatism in the northern Tanzanian mantle: petrographic and geochemical characteristics, *Earth planet. Sci. Lett.,* **114**(4), 463–475.
Sakkas, V., Meju, M., Khan, M., Haak, V. & Simpson, F., 2002. Magnetotelluric images of the crustal structure of Chyulu Hills volcanic field, Kenya, *Tectonophysics,* **346,** 169–185.
Saria, E., Calais, E., Altamimi, Z., Willis, P. & Farah, H., 2013. A new velocity field for africa from combined GPS and DORIS space geodetic solutions: contribution to the definition of the African reference frame (AFREF), *J. geophys. Res.,* **118**(4), 1677–1697.
Seht, M.I., Blumenstein, S., Wagner, R., Hollnack, D. & Wohlenberg, J., 2001. Seismicity, seismotectonics and crustal structure of the southern Kenya Rift-new data from the Lake Magadi area, *Geophy. J. Int.,* **146**(2), 439–453.
Selway, K., 2015. Negligible effect of hydrogen content on plate strength in East Africa, *Nat. Geosci.,* **8**.
Selway, K., Yi, J. & Karato, S., 2014. Water content of the Tanzanian lithosphere from magnetotelluric data: Implications for cratonic growth and stability, *Earth planet. Sci. Lett.,* **388,** 175–186.
Simpson, F., 2000. A three-dimensional electromagnetic model of the southern Kenya Rift: departure from two dimensionality as a possible consequence of a rotating stress field, *J. geophys. Res.,* **105**(B8), 19 321–19 334.
Sleep, N.H., Ebinger, C.J. & Kendall, J.-M., 2002, Deflection of mantle plume material by cratonic keels, *Geol. Soc., Lond., Spec. Publicat.,* **199,** 135–150.
Stamps, D.S., Saria, E. & Kreemer, C., 2018. A geodetic strain rate model for the East African Rift system, *Nat., Scient. Rep.,* **8,** 732.
Steck, L. & Prothero, W., 1991. A 3-d raytracer for teleseismic body-wave arrival times, *Bull. seism. Soc. Am.,* **81**(4), 1332–1339.
Sun, M., Liu, K.H., Fu, X. & Gao, S.S., 2017. Receiver function imaging of mantle transition zone discontinuities beneath the Tanzania craton and adjacent segments of the East African Rift system, *Geophys. Res. Lett.,* **44,** 12 116–12 124.
Takei, Y., 2002. Effect of pore geometry on vp/vs: From equilibrium geometry to crack, *J. geophys. Res.,* **107**(B2), ECV 6–1–ECV 6–12.
Thompson, D.A., Hammond, J.O.S., Kendall, J.-M., Stuart, G.W., Helffrich, G.R., Keir, D., Ayele, A. & Goitom, B., 2015. Hydrous upwelling across the mantle transition zone beneath the Afar triple junction, *Geochem. Geophys. Geosyst.,* **16**(3), 834–846.
Tiberi, C. *et al.*, 2000. Crustal and upper mantle structure beneath the Corinth rift (Greece) from a teleseismic tomography study, *J. geophys. Res.,* **105,** 28159–28172.
Tiberi, C., Diament, M., Caen, H.L. & King, T., 2001. Moho topography beneath the Corinth rift area (greece) from inversion of gravity data, *Geophys. J. Int.,* **145**(3), 797–808.
Tommasi, A. & Vauchez, A., 2001. Continental rifting parallel to ancient collisional belts: an effect of the mechanical anisotropy of the lithospheric mantle, *Earth planet. Sci. Lett.,* **185,** 199–210.
van Wijk, J., van Hunen, J. & Goes, S., 2008. Small-scale convection during continental rifting: evidence from the Rio Grande rift, *Geol. Soc. Am.,* **36**(7), 575–578.
VanDecar, J.C. & Crosson, R.S., 1990. Determination of teleseismic relative phase arrival times using multi-channel cross-correlation and least squares, *Bull. seism. Soc. Am.,* **80**(1), 150.
Vauchez, A., Dineur, F. & Rudnick, R., 2005. Microstructure, texture and seismic anisotropy of the lithospheric mantle above a mantle plume: insights from the Labait volcano xenoliths (Tanzania), *Earth planet. Sci. Lett.,* **232**(3), 295–314.
Weeraratne, D., Forsyth, D., Fischer, K. & Nyblade, A.A., 2003. Evidence for an upper mantle plume beneath the Tanzanian craton from Rayleigh wave tomography, *J. geophys. Res.,* **108**(B9), 2427.
Weinstein, A. *et al.*, 2017. Fault-magma interactions during early continental rifting: seismicity of the Magadi-Natron-Manyara basins, Africa, *Geochem. Geophys. Geosyst.,* **18**(10), 3662–3686.
Wendlandt, R. & Morgan, P., 1982. Lithospheric thinning with rifting in East Africa, *Nature,* **298,** 734–736.
West, M., Ni, J., Baldridge, S., Wilson, D., Aster, R., Gao, W. & Grand, S., 2004. Crust and upper mantle shear wave structure of the southwest United States: implications for rifting and support for high elevation, *J. geophys. Res.,* **109**(B03309), doi:10.1029/2003JB002575.
Wheildon, J., Morgan, P., Williamson, K., Evans, T. & Swanberg, C., 1994. Heat flow in the Kenya Rift zone, *Tectonophysics,* **236**(1-4), 131–149.
Yang, Z. & Chen, W., 2010. Earthquakes along the East African Rift system: a multiscale, system-wide perspective, *J. geophys. Res.,* **115**(B12309), doi:10.1029/2009JB006779.
Zeyen, H. & Achauer, U., 1997. Joint inversion of teleseismic delay times and gravity anomaly data for regional structures: theory and synthetic examples, in *Upper Mantle Heterogeneities from Active and Passive Seismology,* pp. 155–168, ed. Fuchs, K., Kluwer Acad.

SUPPORTING INFORMATION

Supplementary data are available at *GJI* online.

Figure S1. Result from synthetic test with two localized −5 per cent anomalies in layer 2 (40 km depth), for (a) the density contrast and (b) the velocity anomaly. The input anomaly location and shape are marked by the thin black rectangles. The transparency mask in (a) indicates zones not constrained by seismic rays.
Figure S2. Result from synthetic test with two localized −5 per cent anomalies in layer 5 (185 km depth), for (a) the density contrast and (b) the velocity. The input anomaly location and shape are marked by the thin black rectangles. The transparency mask in (a) indicates zones not constrained by seismic rays.
Figure S3. Result from synthetic test with two localized −5 per cent anomalies at 300 km depth, deeper than our model limits. The input anomaly location and shape are marked by the thin black rectangles and reported on the last layer. (a) Results for the density contrast, with a transparency to indicate zones not constrained by seismic rays. (b) Results for the velocity anomaly.
Figure S4. Output density model from synthetic test with a single −5 per cent anomalies from 80 to 300 km depth. The input anomaly location and shape are marked by the thin black line. The transparency mask indicates zones not constrained by seismic rays.
Figure S5. Output velocity model from synthetic test with a single −5 per cent anomalies from 80 to 300 km depth. The input anomaly location and shape are marked by the thin black line.

Please note: Oxford University Press is not responsible for the content or functionality of any supporting materials supplied by the authors. Any queries (other than missing material) should be directed to the corresponding author for the article.

Downloaded from https://academic.oup.com/gji/article-abstract/216/3/1693/5237708 by guest on 04 January 2019